Maximilian Hehenberger, BSc

"The effect of temperature on deformation mechanisms in ZKQX6000 alloy and pure Mg"

Masterarbeit

zur Erlangung des akademischen Grades

Master of Science

Masterstudium Production Science and Management

eingereicht an der

Technischen Universität Graz

unter der Betreuung von

Assoc. Prof. Dr. techn. Univ.-Doz. Maria Cecilia Poletti

Institut für Werkstoffkunde und Schweißtechnik, TU Graz

und

Dr. Chamini Mendis und Dr. techn. Domonkos Tolnai

Magnesium Innovation Center, Helmholtz-Zentrum Geesthacht

Graz, Juli 2014

Eidesstattliche Erklärung

Affidativ

Ich erkläre an Eides statt, dass ich die vorliegende Arbeit selbstständig verfasst, andere als die angegebenen Quellen/Hilfsmittel nicht benutzt, und die den benutzten Quellen wörtliche und inhaltlich entnommene Stellen als solch kenntlich gemacht habe. Das in TUGRAZonline hochgeladene Textdokument ist mit der vorliegenden Masterarbeit identisch.

I declare that I have authored this thesis independently, that I have not used other than the declared sources/resources, and that I have explicitly indicated all material which has been quoted either literally or by content from the sources used. The text document uploaded to TUGRAZonline is identical to the present master`s thesis.

Datum / Date

Unterschrift / Signature

Acknowledgement

At the end of my thesis I would like to thank all the persons who made this thesis possible and a memorable experience for me.

I wish to thank, first and foremost, my supervisors Prof. Cecilia Poletti from the IWS institute at the TUGraz, Dr. Chamini Mendis and Dr. Domonkos Tolnai from the Magnesium Innovation Centre at the HZG for supporting me. I want to thank them for the great guidance and effort they put into training me in the material science field.

I acknowledge my gratitude to Prof. Dr. Ulrich Kainer and Dr. Norbert Hort for giving me the opportunity to be a part of the “MagiC-Team” and to Frau Petra Fischer and Herrn Gert Wiese for the technical assistance to my project.

A special thanks also to Prof. K.S. Shin and Prof. K. Hono from the Magnesium Innovation Center at the Seoul National University, who provide the tested specimens.

I am thankful to my colleagues Herrn Cesar Stüpp and Herrn Ricardo Henrique Buzolin for the spiritual support and precious friendship during my stay in Germany.

Finally, I want to express my sincere thanks also to my beloved parents, Mag. Daniela Stein and Dipl.-Ing. Gerald Hehenberger, for their understanding, continual support – both spiritually and materially - and for giving me the motivation to choose studies in a technical field.

Abstract

This master thesis is dealing with the effect of temperature on deformation mechanisms in pure Mg and ZKQ6000 alloy. The ZKQX6000 alloys have reported to show a good combination of yield strength, ductility and formability, but the process of deformation had not been sufficiently clarified.

In this work different experimental methods are be used to show the basic differences in deformation between the pure Mg and the ZKQX6000 alloy. The investigations are restricted to room temperature and 250°C and in each case to a deformation up to 0.05, 01 and 0.3 of strain. EBSD and LOM analyses are conducted to investigate the materials in terms of developed grain size and crystal misorientation to describe twinning and dynamic recrystallization. In addition, azimuthal-angle/time plots and the change in intensities of the *in situ* synchrotron diffraction patterns are observed to investigate deformation processes in "*real time*". Concluding, the results of the pure Mg and the ZKQX6000 alloy are compared and explained by the current state of the scientific investigations.

Keywords: *Mg; ZKQX6000 alloy; in situ compression; synchrotron diffraction; EBSD, DRX; twinning*

Kurzfassung

Diese Masterarbeit beschäftigt sich mit dem Temperatureinfluss auf Deformationsprozesse in reinem Mg und der Legierung ZKQX6000. Die ZKQX6000 Legierung weist eine gute Kombination zwischen Fließfestigkeit, Zähigkeit und Verformbarkeit auf, jedoch sind die genauen Deformationsprozesse die zu diesen Eigenschaften führen noch größtenteils ungeklärt.

In dieser Arbeit werden verschieden experimentelle Methoden vorgeführt und die elementaren Unterschiede zwischen reinem Mg und der ZKQX6000 Legierung untersucht. Die Versuche beschränken sich jeweils auf Raumtemperatur und 250°C und einem Umformgrad von 0.05, 0.1 und 0.3. Eine EBSD und lichtmikroskopische Analyse wird durchgeführt, um die Proben auf Korngröße, Zwillingsbildung und dynamischer Rekristallisation zu untersuchen. Des Weiteren werden azimuthal-angle/time plots und die Änderung der Intensitäten der *in situ* Synchrotron Diffraktion untersucht, um die Deformationsprozesse in „Echtzeit“ zu beobachten.

Abschließend werden die Ergebnisse des reinen Mg und der ZKQX6000 Legierung verglichen und mit Hilfe dem Stand der Technik erklärt.

List of Abbreviation

A	Working surface [m^2]
A( )	Amplitude
a_i	Base vectors
A-T	Azimuthal-angle/time
BKD	Backscatter Kikuchi Diffraction
c	Phase speed [λ/T]
CDRX	Continuous dynamic recrystallization
CRSS	Critical resolved shear stress
DDRX	Discontinuous dynamic recrystallization
d_{hkl}	Distance between diffracted planes
DRX	Dynamic recrystallization
EBSD	Electron backscatter diffraction
EDX	Energy Dispersive X-Ray
f	Frequency [Hz]
F_s	Structure factor
F	External force [N]
f_p	Atomic form factor
GROD	Grain orientation deviation
GROD	Grain reference orientation deviation
HAGB	High angle grain boundary
I	Intensity
IPF	Inverse pole figures
k	Wave number [$\lambda/2\pi$]

K	Difference of wavenumbers
KAM	Kernel average misorientation
λ_w	Wave length [c/f]
λ	Angle between force and slip direction [degree]
LAGB	Low angle grain boundary
LD	Loading direction
LTDR	Low temperature dynamic recrystallization
m	Orientation factor
n_i	Integers of base vectors
OIM	Orientation Imaging Microscopy
OP-S	Colloidal silica solution
R_n	Vector pointing the unit cell
r_p	Position vector pointing the atom in the unit cell
SEM	Scanning electron microscopy
TD	Transverse direction
TDRX	Twin dynamic recrystallization
κ	Angle between force and normal direction [degree]
σ	Stress [N/m^2]
$\sigma_{o.2}$	Yield stress at 0.02 of strain [MPa]
τ	Resolved shear stress [N/m^2]

Table of content

1 Introduction

With a density of 1.74 g/cm^3 Mg is the lightest metal for structural applications. Mg alloys are attractive due to their low density and ease of casting and machinability. Although there was a significant increase in its use 70 years ago (Polmear 2006) , Mg disappeared largely from the array of products due to the complexity of processing and associated costs. Since some years Mg alloys experience a renaissance in different areas and the production in China (97% of the world market) of Mg alloys shows a growth of over 43 % (Jinxiang 2014) in the last year. Particularly, the automobile and aircraft industries focus on Mg alloys to reduce the weight and to ensure the environmental sustainability through fuel efficiency. Furthermore, the electronic industry contributes to the light metal´s upturn. High quality plastic cases of laptops or mobile phones are increasingly replaced with Mg alloys.

The environmental advantage of Mg alloys is clearly exhibited in the transport applications. A large percentage of the yearly CO_2 emissions are produced by road and rail transport vehicles. In 2008 the European Union adopted a law forcing the automotive industry to reduce the CO_2 emissions to 95 g/km until 2020. (BMU 2010) Therefore, the easiest way to reach this target is by the reduction in weight, where Mg and its alloys could play a central role.

Today, many Mg alloy parts are produced by die-casting for commercial applications. However, their mechanical strength at room temperatures and their mechanical resistance at elevated temperatures do not fulfil the advanced requirements of components.(Yin et al. 2005)

Presently around up to 6 kg Mg are incorporated in one car. Experts believe that by the year 2020 there will be an increase of about 100 kg of magnesium per car (Brünglinghaus 2012). Therefore, to sustain the demand of load bearing applications, magnesium alloys with higher strength and toughness have to be developed.

In this present work the deformation behaviour at room temperature and 250°C was investigated for pure Mg and ZKQX6000 alloy with a composition of Mg- 6Zn-0.4Ag-0.2-Ca-0.6Zr (wt.%). The ZKQX6000 alloys have reported to show a good combination of yield strength, ductility and formability in the wrought state showing commercial potential (Mendis et al. 2009).

2 Motivation

Mendis et al. (Mendis & Hono 2007; Oh-ishi et al. 2009; Mendis et al. 2009) reported that the extruded and heat-treated Mg- 6Zn-0.4Ag-0.2-Ca-0.6Zr (wt%) has a yield strength of 325 MPa and an ultimate tensile strength of 360 MPa after T6 heat treatment (solution treated 30min/400°C and aged 72h/160°C). In comparison, a conventionally rolled AZ31 (Mg- 3Al-0.5Zn (at%)) shows lower properties with a yield strength of 235 MPa.

Many Mg alloys such as wrought AZ31 (Barnett 2004) show a similar deformation behaviour to that of pure Mg. This is exhibited by the large anisotropy in tensile and compression yield strengths. The ratio between compression and tensile yield strengths can vary between 0.3-0.6 in AZ31 and ZK60 alloys (Koike 2003). On the other hand, ZKQX6000 alloy has relatively isotropic yield strengths in as-extruded condition with compressive yield strength being 0.85 of the tensile yield strength (Mendis et al. 2009). The relatively isotropic behaviour exposed by ZQKX6000 alloy suggests that there might be significant differences in the activation of the deformation modes in ZKQX6000 alloys as compared with pure Mg.

For all the exposed above, it is of interest to compare deformation behaviour of ZKQX6000 alloy with that of pure Mg at room temperature and at 250°C, especially in compression where high density of twinning is generally observed in conventional alloys.

3 State of the art

3.1 Crystal structure of magnesium

Mg has a hexagonal close packed (hcp) crystal structure that consists of different layers of atoms, as shown in Figure 3.1. The first layer of this structure has the position “B”, followed by the second with position “A”. The third layer is identical with the first one, so that the stacking sequence becomes ….BABABABA…(Gottstein 2007)

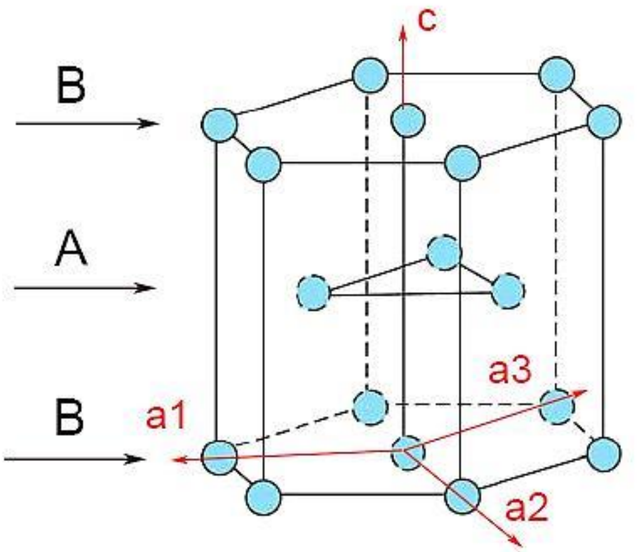

Figure 3.1: Stacking sequence of a hcp lattice (Moffatt 1964)

Figure 3.1 shows the two axes *a* and *c* with different lengths, of a = 0.32 nm and c = 0.52 nm. The base of this structure is called basal plane (position “B”) and is formed by the axes a_1, a_2 and a_3 with the same dimension. The orientation of the *c* axis is normal to the basal plane. Magnesium has a c/a ratio of 1.623, close to the ideal value of 1.633.

3.1.1 Characterisation of crystallographic planes and directions

The Miller indices indicate the crystallographic planes and directions of a crystal structure. The values (hkl) represent the points of intersection of the crystal planes with the Cartesian axes x, y and z. However, for hexagonal crystal structures the Miller Bravais notations are used in addition to the Miller indices where (hkil) represents the intersection points with 4 axes, which allow conservation of the hexagonal structure.

These values are the integer numbers of the reciprocal value of the axes a_1, a_2, a_3 and c. The big advantage of the Miller Bravais indices for hexagonal structured materials is that the crystallographic equivalent planes are described with equivalent indices. For example in Figure 3.2 the two planes ADEB and A´D´DA are crystallographic equivalent, but they are illustrated by different Miller- Indices (100) and $(1\bar{1}0)$. On the contrary the Miller Bravais indices are $(10\bar{1}0)$ and $(1\bar{1}00)$. (Gottstein 2007)

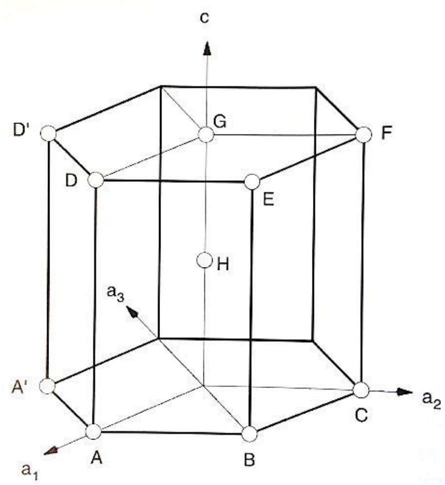

Figure 3.2: Orientation of basal, prismatic and pyramidal planes (Gottstein 2007)

Basal plane: e.g. (DEFG)

Prismatic planes:

  1st type: (e.g. ABED)

  2nd type : (e.g. ACFD)

Pyramidal planes:

  1st type : 1st Order (e.g. ABG)

  1st type : 2nd Order (e.g. ABH)

  2nd type : 1st Order (e.g. ACG)

  2nd type : 2nd Order (e.g. ACH)

The Miller Braivais Indices can be converted in the Miller-Indices and vice versa (Gottstein 2007):

For planes: (hkl) → hkil = (h, k, - (h + k), l)

For directions: [uvw] → [uvtw] = [2u – v, 2v – u, - (u+v), 3w]

The planes in a crystal structure are characterised by parenthesis ( ), while their directions are characterised by brackets [ ]. Additionally, planes and directions which are crystallographic equivalent, as already mentioned above, are described by { } for planes and < > for directions. By convention, negative integers are written with a bar, as in $\bar{1}$ for -1. Figure 3.3 shows the principal directions in a magnesium unit cell.

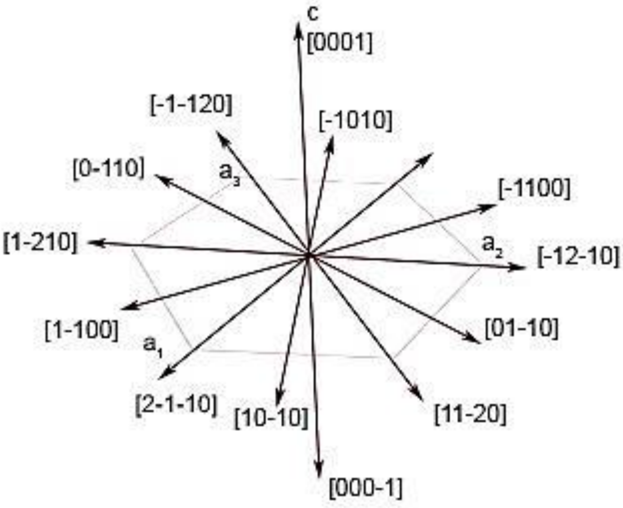

Figure 3.3: Principal directions in the magnesium unit cell (Polmear 2006)

3.2 Plastic deformation of Mg and its alloys

An elongation to failure in tension of only 10% (Agnew et al. 2001) can be reached in pure homogenised Mg at room temperature (RT). This low value based on the fact that a metal with hcp structure does not meet the criterions of Taylor (Taylor 1938) at RT for plastic deformation. The Taylor criterion states that at least five independent slip systems are required for the accommodation of the plastic strain. It says that the change in volume of a cylindrical sample stays constant while deforming and thus 5 out of 6 tensor vectors are taken in consideration, based on the von Mises criterion (von Mises 1928). In pure Mg there are only 2 independent slip systems available at RT. Therefore, other deformation mechanisms such as twinning are needed to reduce the strain.

There a two main mechanism for plastic deformation: crystallographic slip and twinning.

3.2.1 Dislocation slip

The formation and movement of dislocations through compact crystallographic planes in slip directions is one of the most important deformation mechanisms for ductile metals. The shear occurs along close packed planes and causes the deformation of the crystal. When the resolved shear stress rises above a certain value dislocation motion is initiated. This boundary value is called critical resolved shear stress (CRSS). The Figure 3.4 illustrates the slip direction and planes during simple tension. The formula below (**1**) shows the relationship in a monocrystal of this shear stress with the orientation of the slip plane, the slip system and the external applied force (Schmid 1968):

$$\boldsymbol{\tau = \frac{F}{A} \cdot (cos\lambda \cdot \mathbf{cos\kappa}) = \sigma \cdot m} \tag{1}$$

where F is the external force, A the section of the system exposed to this force, λ the angle between the force and the slip direction and k the angle between the normal direction of the slip plane and the force. The m stands for the orientation factor, which is the maximum value of the term ($\cos\lambda\cos\kappa$). In polycrystalline material the slip system with the highest orientation factor will be deformed preferentially. (Schmid 1968)

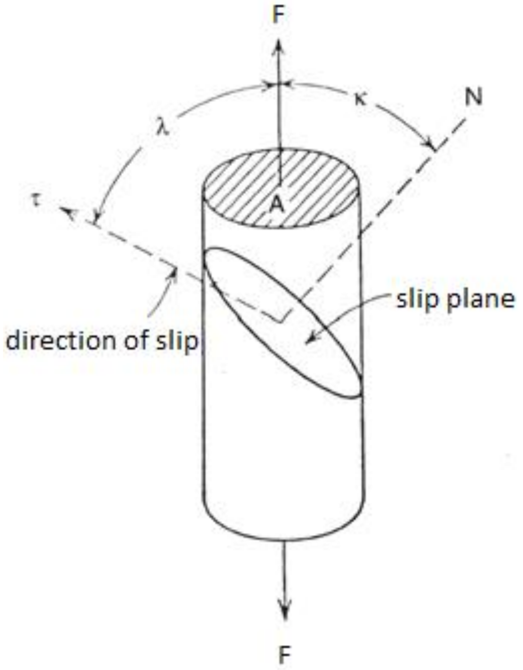

Figure 3.4: Slip direction and slip plane (Gottstein 2007)

An overview of the possible slip systems for magnesium is shown in Table 3.1:

Table 3.1: Crystallographic indices of the slip and twinning planes and directions of Mg (Yoo 1981)

Planes	Directions	Type	Slip direction[1]	Number of independent systems
(0002)	$\langle 11\bar{2}0 \rangle$	Basal	<a>	2
$\{10\bar{1}0\}$	$\langle 11\bar{2}0 \rangle$	Prismatic	<a>	2
$\{10\bar{1}1\}$	$\langle 11\bar{2}0 \rangle$	Pyramidal	<a>	4
$\{11\bar{2}2\}$	$\langle 11\bar{2}3 \rangle$	Pyramidal	<c + a>	5

---

[1] Slip Directions in an hcp lattice are shown in Figure 3.3

Compared to cubic crystals there are fewer independent slip systems available in hexagonal crystals. The activation of available slip systems depends on the c/a ratio of the material. Lager slip vectors or less densely packed slip planes hinder the dislocation movement. The basal slip in the closest packed direction <11$\bar{2}$0> (3 directions), in the closest packed basal plane (0002) is the easiest activated slip system in Mg (Al-Samman 2008).

The activation of the slip systems depends strongly on the temperature. Therefore, the crystallographic behaviour is analysed as a function of the deformation temperature.

RT:

According to Roberts (Roberts 1964) there are only 2 independent slip systems available for pure Mg at RT, both involving the (0001) <11$\bar{2}$0>-basal slip system. According to the Taylor´s criterion a minimum of five independent slip systems have to be available to allow homogeneous, generalized ductility of a polycrystalline material.

Therefore, in Mg alloys to allow homogeneous deformation, also mechanical twinning occurs, which offers an additional half of an independent deformation mode, leading to a total of 2 $\frac{1}{2}$ independent slip systems.

Elevated temperature:

Mg alloys exhibit low ductility near RT due to their limited number of active slip systems having an hcp crystal structure. In order to obtain the adequate ductility required for plastic forming, Mg alloys need to be deformed above 220°C to activate non-basal slip systems. (Akhtar & Teghtsoonian 1969a)

With elevated temperature, prismatic ({10$\bar{1}$0} <11$\bar{2}$0>) and pyramidal slip ({10$\bar{1}$1} <11$\bar{2}$0>) are activated at lower stresses. Similar to the basal slip, the prismatic slip can be divided into three slip systems with only two independent ones (see Figure 3.5 (a) and (b)). The pyramidal slip occurs on two different planes, the Type 1 ({10$\bar{1}$1} and {10$\bar{1}$2}, in <11$\bar{2}$0> direction, see Figure 3.5 (c)), offering four independent slip systems, and Type 2 ({11$\bar{2}$2}, <11$\bar{2}$3>), leading to a total of five independent slip systems, see Figure 3.6. Due to the different slip vectors, Type 1 of pyramidal slip is called <a> slip and the pyramidal slip of the Type 2 <c+a> slip. (Yoo 1981)

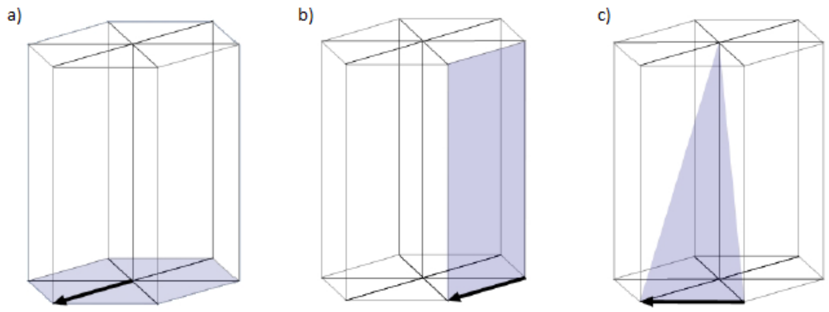

Figure 3.5: Slipping direction of (a) basal slip (0001)<11$\bar{2}$0> (b) prismatic slip {10$\bar{1}$0}<11$\bar{2}$0> (c) pyramidal slip {10$\bar{1}$1}<11$\bar{2}$0> (Müller 2007)

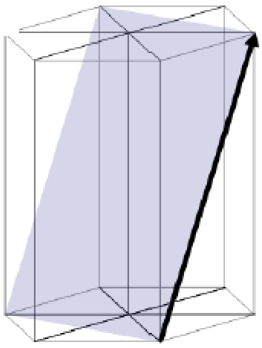

Figure 3.6: Type 2 of pyramidal slip {11$\bar{2}$2}<11$\bar{2}$3> with five independent slip systems (Müller 2007)

3.2.2 Mechanical twinning

In addition to dislocation slip, mechanical twinning plays an important role during plastic deformation, especially at RT. The twinning leads to a rotation of a crystal and activates slip systems that were inactive before. Twinning is a process in which part of a crystal is rotated symmetrically under the influence of shear stress. A mirror plane is created between the twin and the matrix which is called coherent twinning plane. (Gottstein 2007) In order to reduce the strain at the grain boundaries, mechanical twinning can nucleate where sufficient five independent slip systems do not exist to accommodate the strain. (Yoo 2002)

The mechanical twinning differs in three aspects from the deformation mechanism carried out by dislocation. Firstly, it is unidirectional. This means that twins can only generate either by tensile or a compressive strain along the c-axis. The most common twinning mechanism in hcp metals involves shear stress along the {10$\bar{1}$2} planes in <10$\bar{1}$1> direction, and is known as tensile twinning, operating parallel to the c-axis for a c/a ratio <√3. The second difference with respect to slip of dislocation is that the strain accommodation is limited. Thus, mechanical twinning can only accommodate a fixed amount of shear strain and $\{10\bar{1}2\}$ twinning occurs with a very low amount of shear stress. The third aspect is the sudden reorientation of the crystals. Planes orientated vertical to the basal one after a $\{10\bar{1}2\}$ twinning, rotates by 86.3° in $<11\bar{2}0>$ direction and are reoriented close to the basal orientation. Therefore, the new created twins are able to activate new slip systems and further twinning. (Gottstein 2007)

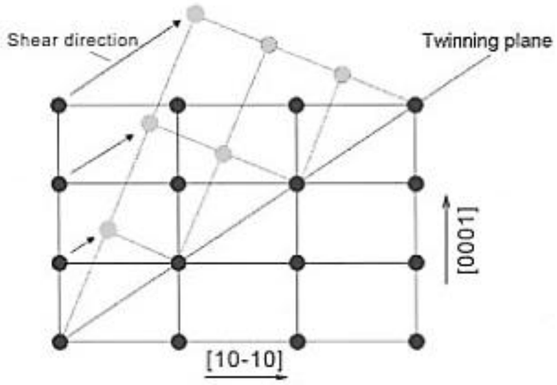

Figure 3.7: Mechanical twinning process with initial position of atoms (black points)and their final position after twinning (grey points) (Gottstein 2007)

Yoo et al. (Yoo 1981) found that the local stress concentration between the interaction of certain slip dislocations can create new twins or a crack. Additionally, Barnett (Barnett 2004) reported the process of *twinning- induced hardening*. It describes that the newly formed twin boundaries act similar to a grain boundary as an auxiliary barrier for dislocation movement producing work hardening.

3.2.2.1 Tension twinning-{10-12} <10-11>

The tension twinning, also called extension twinning, is the most common twinning mechanism observed in Mg. The name tension twin derives from the resulting extension in the direction of applied stress. This mechanism is illustrated in Figure 3.8, where the position “I” in the un-twinned crystal becomes position “T” following tensile twinning and elongating the length of the resulting crystal in the direction of the applied force. The tension twins arise in $\{10\bar{1}2\}$ planes and in $<10\bar{1}1>$ direction, leading to a rotation of the crystal by 86.3°. As a function of the c/a ratio twinning vertical to the basal plane results in either an extension (c/a < 1.73) or a contraction (c/a > 1.73). (Gottstein 2007)

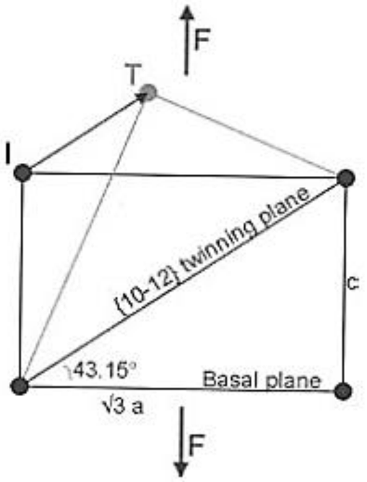

Figure 3.8: Process of tension twinning (Gottstein 2007)

3.2.2.2 Compression twinning-{10-11} <10-12>

This form of twinning results in a compression instead of a tensile strain along the c-axis, as illustrated in Figure 3.9. Unlike tension twinning, $\{10\bar{1}1\}$-twins are often observed near to the fracture zone, have a different morphology and are hard to detect. This twinning system includes $\{10\bar{1}1\}$ and $\{10\bar{1}3\}$-twins in $<10\bar{1}2>$ direction and can also be activated by an extension orthogonal to the c- axis. The rotation angle is 56.2° and the basal plane is rotated in the same $<11\bar{2}0>$-direction, similar to tension twinning. (Al-Samman 2008) The compression twins, in contrast to the tension twins, are thin and therefore their identification by the EBSD-technique is hard. (Barnett 2007)

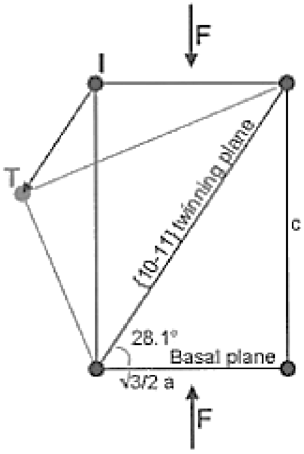

Figure 3.9: Process of compression twinning (Gottstein 2007)

3.2.2.3 Double twinning-{10-11} {10-12}

Double twinning is referred to compression as well as tension twinning that appears in an interlaced manner, meaning that $\{10\bar{1}1\}$-compression twins take place firstly and that a $\{10\bar{1}2\}$-tension twins occur inside. The result is a 37° rotation angle with reference to the basal plane of the un-twinned matrix. Wonsiewicz et al. (Wonsiewicz & Backofen 1967) found that due to $\{10\bar{1}1\}$-$\{10\bar{1}2\}$- double twinning a special adjustment of the basal planes inside the twins occurs, leading to slip activation. Thereby, high localized strains, softening and internal failure occur within double twins.

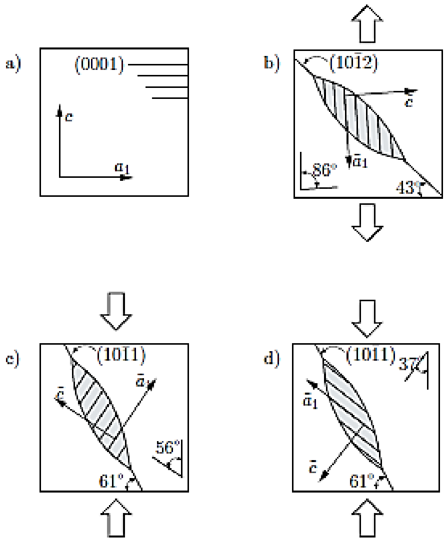

Figure 3.10: Rotation of basal planes due to twinning, a) initial crystallographic directions c and a_1, b) lenticular presents the tensile twinning, c) contraction twinning, d) double twinning (Homayonifar 2011)

Figure 3.10 illustrates the rotation process of basal planes due to double twinning. Whereas tensile twinning leads to an increase of the uniform elongation, $\{10\bar{1}2\}$-double twinning might be accountable for a decrease in ductility with the formation of voids and strain softening. (Barnett 2007)

3.2.3 Activation of slip and twinning in magnesium

The critical resolved shear stress (CRSS) is crucial for the activation of the different slip and twinning systems in pure Mg and its alloys.

There is a relationship between the c/a ratio and the CRSS ease of activating dislocation, as shown in Table 3.2. The basal slip for pure Mg with an almost ideal c/a ratio occurs at a low CRSS, while in other hcp metals such as in Zn with a c/a ratio far from the ideal, the activation of basal slip requires a much higher CRSS.

Table 3.2: A comparison of CRSS levels for basal planes and c/a ratios for different metals with hcp crystallography (25°C) (Gottstein 2007)

Metal	CRSS (MPa)	c/a
Mg	0.4344	1.623
Cd	0.5653	1.886
Zn	110.32	1.588
Be	39.3	1.586

Table 3.3 (Lou et al. 2007) shows that basal slip has the lowest CRSS for pure magnesium ranging from 0.45 to 0.81 MPa. Twinning has a CRSS two to four times larger than basal slip, and prismatic slip has a significantly larger CRSS. Additionally, it is shown that with the addition of a small percentage of Zn the activation energy for twinning increases.

In pure Mg due to the small CRSS required for basal slip, prismatic and pyramidal slips are only activated in areas with a high local concentration of stress. (Al-Samman 2008)

Table 3.3: CRSS reported for pure magnesium at RT (Lou et al. 2007)

Metal	Condition	$CRSS_{basal}$ (MPa)	$CRSS_{twin}$ (MPa)	$CRSS_{prim}$ (MPa)	$CRSS_{twin}$/ $CRSS_{basal}$	$CRSS_{prism}$/ $CRSS_{basal}$
Pure Mg	single crystal	0.81[1]; 0.76[2]; 0.45[3]; 0.65[4]; 0.52[5]	2[6]	39[6]	2.5 - 4.4[6]	48 – 87[6]
Mg-0.5Zn (at%)	single crystal		2.7-2.8[7]			

[1] Schmid (1931)

[2] Bakarian and Mathewson (1943)

[3] Burke and Hibbard (1952)

[4] Hsu and Cullity (1954)

[5] Conrad and Robertson (1957)

[6] Reed-Hill and Robertson (1957)

[7] (Lou et al. 2007; Miura 2004)

Figure 3.11 shows the CRSS for various slip systems in pure Mg. At low temperatures the prismatic slip requires a very high CRSS for activation. As the temperature is increased, the CRSS for activation for prismatic and pyramidal slip decreases. The basal slip shows a relatively constant CRSS over a wide temperature range. Because twinning is an athermal process the related CRSS is not dependent on the temperature.

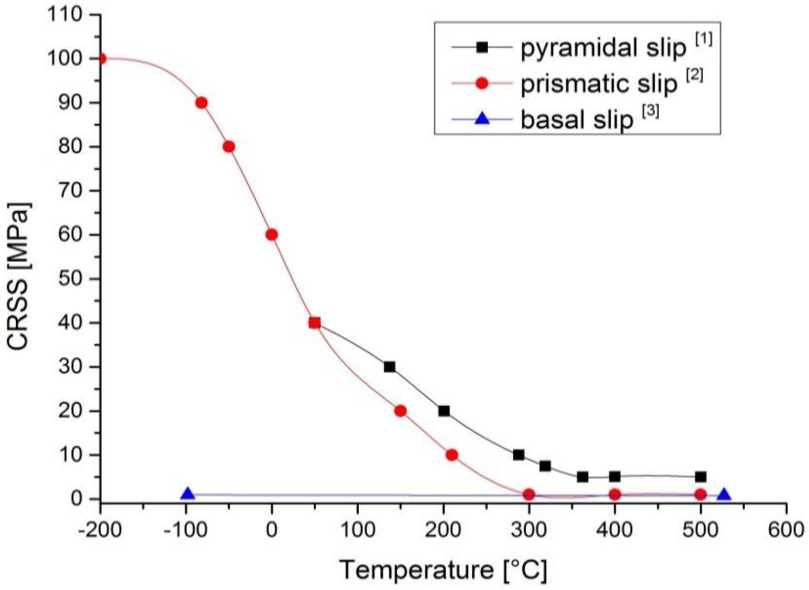

Figure 3.11: The CRSS for various slip systems of pure Mg adapted from [1](Obara 1973) [2](Ion 1982) [3](Raynor 1959)

The CRSS for the activation of various slip systems are affected by the addition of alloying elements, modifying the deformation mechanism with respect to that of the pure metal. Since the main alloying addition in the ZKQX6000 alloy investigated is Zn, its effect on the CRSS for basal and prismatic slip is discussed. Akthar (Akhtar & Teghtsoonian 1969a; Akhtar & Teghtsoonian 1969b) reported about the effect of Zn on the activation of basal and prismatic slip.

Figure 3.12 illustrates the dependence of CRSS and temperature for basal slip for different Mg-Zn alloys. The strengthening effect due to increased solute content is observed at RT. Akhtar et al. have observed that there is no significant solution hardening effect above 60°C when the solute content was less than 0.025 at. %. They observed that there is a increment in CRSS with the addition of Zn. As temperature is increased, the CRSS for basal slip decreases for all Zn concentrations and the decrease is more significant for higher Zn contents.

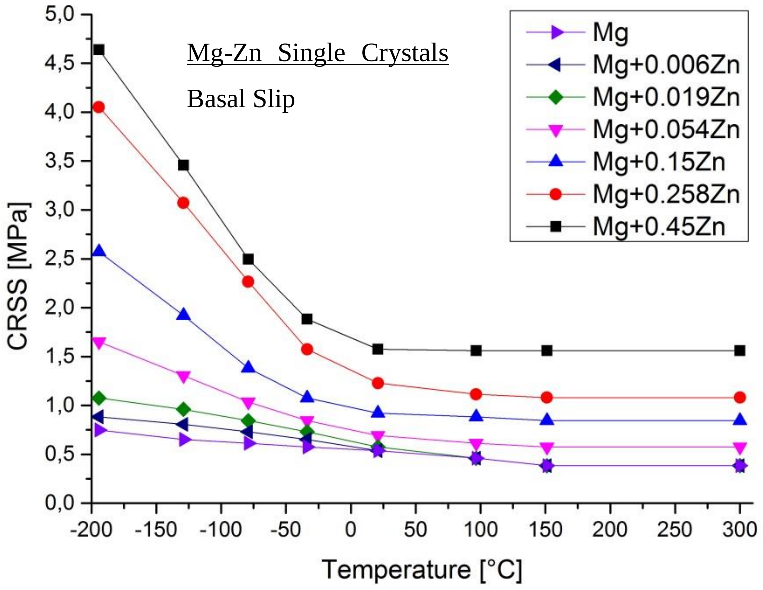

Figure 3.12: Ratio of CRSS for basal slip and temperature for different Mg-Zn alloys adapted from (Akhtar & Teghtsoonian 1969a)

Figure 3.13 shows that for low temperatures the CRSS for prismatic slip in Mg with small addition of solute remain unaffected and that by increasing the solute a decrease of the CRSS is observed. By increasing the temperature, a relatively high decrease by small addition of solute is observed compared to higher concentrations. At approximately 80°C the CRSS of all alloys is higher than that of pure Mg.

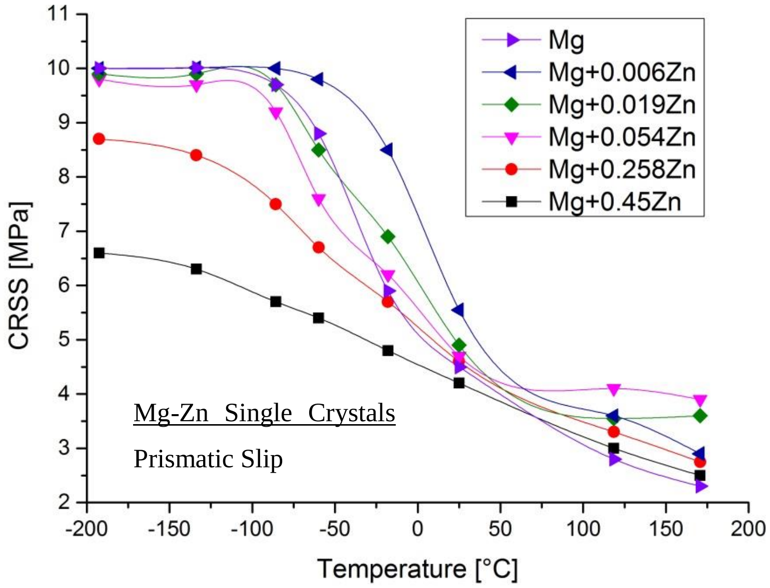

Figure 3.13: Ratio of CRSS for prismatic slip and temperature for different Mg-Zn alloys adapted from (Akhtar & Teghtsoonian 1969b)

Figure 3.14 shows the variation of CRSS in AZ31 for different deformation modes calculated using a visco-plastic model. It is observed that at lower temperatures the CRSS for prismatic and pyramidal slip is much larger than that of the basal slip, whereas the CRSS for twinning shows a mean value. A decrease of the CRSS for twinning was observed at elevated temperatures followed by a drop-off of prismatic and pyramidal slip. In contrast, basal slip is relatively constant over temperature.

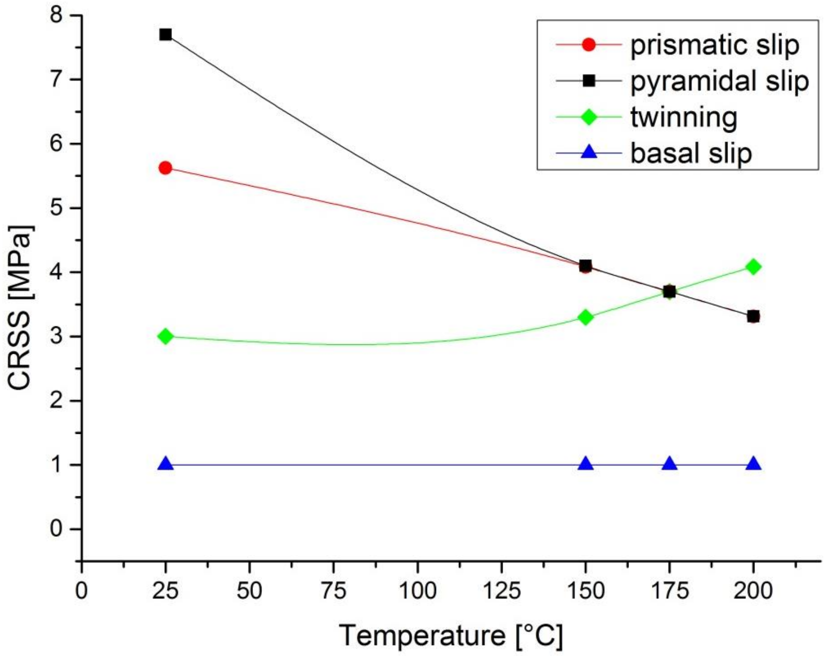

Figure 3.14: Variation of CRSS of AZ31for different deformation modes as a function of temperature adapted from (Jain & Agnew 2007)

3.2.4 Dynamic Recrystallization

The recrystallization occurs when the applied deformation overcomes a critical amount. At hot working, recrystallization can occur during deformation and is called dynamic recrystallization (DRX), lowering the force for deformation and usually increasing the ductility. The DRX is directly linked to the flow stress, so that with an increase in flow stress the resulting grain size becomes smaller. (Gottstein 2007)

Generally the DRX occurs where high local misorientation exists, e.g. (Doherty et al. 1997):

- in existing high angle grain boundaries (>10-15°)
- in high misoriented areas around big particles (d > 1 µm) - grain boundary nucleation (GBN)
- by misorientations through twinning – TDRX (twin DRX) (Sitdikov 2001)

The DRX in Mg and its alloys has been investigated by many groups (Ion 1982) (Galiyev et al. 2001) (Gottstein 2007). There are two types of DRX possible: continuous and discontinuous recrystallization. Ion (Ion 1982) describes the continuous dynamic recrystallization (CDRX) as a recovery process proceeded by an accumulation of strain in low angle grain boundaries. Ultimately this process might result in the formation of high angle grain boundaries and thereby in new grains. However this is a result of a strong recovery process rather than from a classical recrystallization. The other type is the discontinuous dynamic recrystallization (DDRX), and it refers to nucleation and nucleus growth characterized by a high angle grain boundary migration. It should be noticed that in contrast to the CDRX the DDRX shows recrystallized grains with almost no dislocation (Gottstein 2007) (Galiyev et al. 2001).

DRX in pure Mg is observed in a wide temperature range of 0-500 °C. Among others, TDRX, associated with mechanical twinning, occurs at temperatures between 0 and 350 °C and CDRX is observed at a temperature range of 250-500 °C during a steady-state flow. Discontinuous DRX has no significant impact at elevated temperatures and shows a mean recrystallized grain size of 1 µm at low temperatures. This low temperature dynamic recrystallization (LTDRX) takes place, because of strain hardening and the difficulty in rearrangement of the lattice dislocation. (Sitdikov 2001)

Additionally, Galiyev et al. (Galiyev et al. 2001) investigated the recrystallization of Mg alloy ZK60 and found that for low temperatures (T = 150°C) basal <a>-slip and twinning occur frequently. The basal <a>-slips accumulate at the grain and twin boundaries and enhance non-basal slip. This <c+a>-slip promotes the formation of high angle grain boundaries and LTDRX. At elevated temperatures (200-250°C) the <c+a>-slip systems can be activated at grain boundaries more often, leading to a <a>-dislocation cross slip, followed by a formation of low angle grain boundaries. Out of this high angle boundaries are formed, if further dislocation movement is applied (CDRX).

3.3 X-ray synchrotron diffraction and its use in metallic materials

The advantages of the synchrotron diffraction compared to a laboratory device are the high brilliance, the coherence and the tunability of the beam. These characteristics make it possible to penetrate the sample, to get crystallographic information about the bulk, to get a high accuracy and fast measurements. Especially this last characteristic allows the possibility of carrying out *in situ* experiments. *In situ* (on location) means that the measurements are executed, while the sample is deformed or heat treated.

A beamline of a third generation X-ray source is shown in Figure 3.15. In a storage ring with a typical diameter of 300 m, charged electrons or positrons circulate. In the ring bending magnets keep the particles on the trajectory. Furthermore insertion devices like wigglers or undulators consisting of periodically placed dipole magnets force the particles on a periodic path. The acceleration produces the synchrotron radiation. (Als-Nielsen 2010)

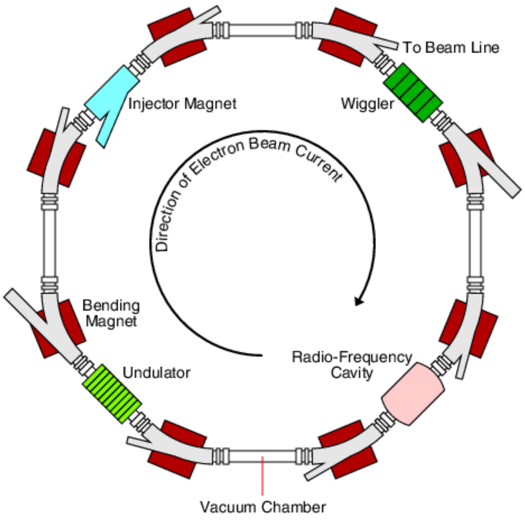

Figure 3.15: Synchrotron storage ring (Barnes 2006)

At synchrotron sources the energy of the beam is usually set high for diffraction experiments in order to penetrate materials up to several mm thicknesses. Therefore, the diffraction experiment is done using the transmission geometry (Figure 3.16), and due to the increased flux of 3rd generation synchrotron sources, the measurement times are about 0.1 sec per data point. (Als-Nielsen 2010)

In situ studies with synchrotron diffraction provide a unique opportunity to investigate the dynamic microstructural processes. As dynamic processes are occurring in the microstructure of the specimen, the morphology of the reflection spots changes. When the diffraction patterns are recorded continuously, grain rotation, sub-grain formation and twinning can be detected during deformation. (Liss, Li, et al. 2009; Liss & Yan 2010; Liss, Yan, et al. 2009; Schmoelzer et al. 2011) To illustrate the development of reflections, thus the microstructure in time, the intensity of one Debye-Scherrer ring (one reflection) is plotted as a function of azimuthal angle and time, shown in Figure 3.16. In these plots (called AT-plots) a stationary reflection spot produces a continuous line.

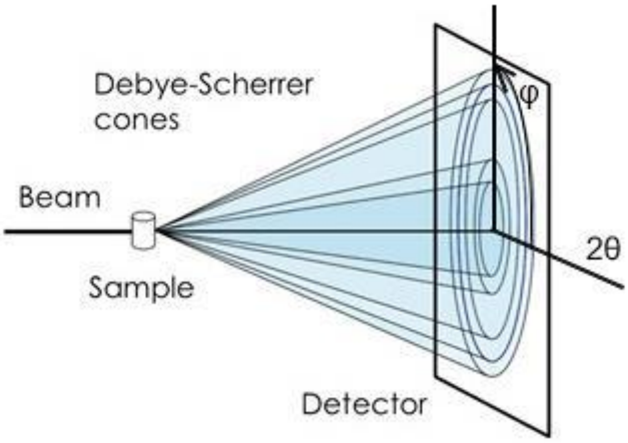

Figure 3.16: Setup of 2D synchrotron diffraction experiment

.

3.4 Kinematical theory of scattering

In this section the theoretical principles of the *in situ* synchrotron diffraction is discussed. The phenomena of X-ray diffraction can be described by the kinematical theory of scattering of diffracted waves hitting atoms in the crystal´s layers. In this description, scattering has the following characteristics:

- the scattering is elastic, so λ (wave length) does not change,
- the scattering is coherent, there is a well-defined phase relation between the inbound wave and the scattered wave for every atom,
- there is no multiple scattering.

In the case of coherent scattering, the interference is determined by the spatial distribution of the scattering centres. If two scattering centres are considered (Figure 3.17) O and P (pointed by the vector r), and a wave with a vector of a wavenumber k_0 strikes them, since the wavelength does not change, the amplitude of the diffracted beam with a vector of wavenumber k is determined by the trajectory difference K coming from these two scattering centres,

$$(\boldsymbol{k_0} - \boldsymbol{k})\boldsymbol{r} = -\boldsymbol{K}\boldsymbol{r}.$$

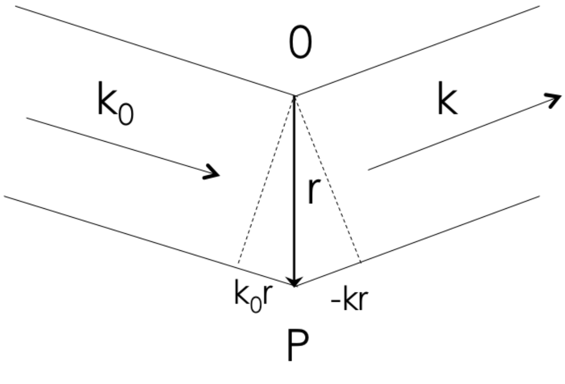

Figure 3.17: Scattering of X-rays in the case of two scattering centres

From this the amplitude A of the diffracted beam can be written as,

$$\boldsymbol{A}(\boldsymbol{K}) = \boldsymbol{A_0}\boldsymbol{e}^{-\boldsymbol{i}\boldsymbol{K}\boldsymbol{r}}. \tag{2}$$

Hence the value of A_0 is identical for all the scattering centres, this term can be disregarded in the geometrical description. In the case of more scattering centres the amplitude can be written as the sum of the amplitudes,

$$\boldsymbol{A}(\boldsymbol{K}) = \sum_{\boldsymbol{n}} \left\{ \sum_{\boldsymbol{P}} \boldsymbol{f_p}\, \boldsymbol{e}^{-\boldsymbol{iKr_p}} \right\} \boldsymbol{e}^{-\boldsymbol{iKR_n}}, \tag{3}$$

where R_n is the vector pointing the cell n, r_p is the position vector of the atom p in the unit cell (Figure 3.18).

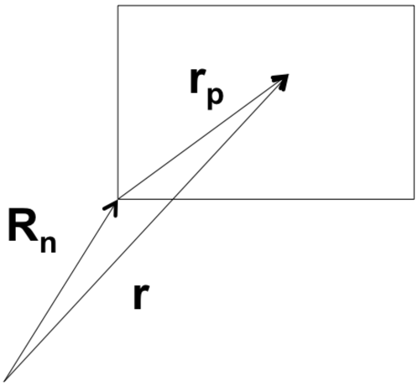

Figure 3.18: Deconvolution of the position vector r of atom P in the unit cell

In the equation (3) the term into brackets is the structure factor (F_s), which describes the scattering of the cell,

$$\boldsymbol{F_s}(\boldsymbol{K}) = \sum_{\boldsymbol{P}} \boldsymbol{f_p}\, \boldsymbol{e}^{-\boldsymbol{iKr_p}}. \tag{4}$$

The scattering of the atom P in the unit cell is considered by the f_p atomic form factor, which is dependent on the electron configuration of the atom, and the angle of scattering. The structure factor considers the structure of the unit cell and the types of atoms. Then, the scattered amplitude can be given as,

$$\boldsymbol{A}(\boldsymbol{K}) = \boldsymbol{F_s}(\boldsymbol{K}) \sum_{\boldsymbol{n}} \boldsymbol{e}^{-\boldsymbol{iKR_n}}. \tag{5}$$

Furthermore, the intensity of the scattered wave equals the square of the absolute value of the amplitude,

$$\boldsymbol{I(K) = |A(K)|^2 = |F_s(K)|^2 \left|\sum_n e^{-iKR_n}\right|^2}. \qquad (6)$$

The term gives a maximum to every K vector, which satisfies any value of R_n, which can be divided by 2π. Every R_n can be written as $n_1a_1+n_2a_2+n_3a_3$, where n_i are integers and a_i are the base vectors of the unit cell. It can be seen that these K vectors satisfy the condition where $K=hb_1+kb_2+lb_3$ where h,k,l are the Miller indices and

$$\boldsymbol{a_i b_j = 2\pi\delta_{ij}}. \qquad (7)$$

The vectors b_1, b_2, b_3 can be expressed as a function of a_1, a_2, a_3 as,

$$\boldsymbol{b_1 = 2\pi\frac{a_1 \times a_3}{a_1(a_2 \times a_3)} \quad b_2 = 2\pi\frac{a_3 \times a_1}{a_2(a_3 \times a_1)} \quad b_3 = 2\pi\frac{a_1 \times a_2}{a_3(a_1 \times a_2)}}. \qquad (8)$$

The crystallographic lattice determined by these vectors is called the reciprocal lattice. In the scattered intensity there is a maximum in these k directions where,

$$\boldsymbol{k - k_0 = g_{hkl}} \qquad (9)$$

where,

$$\boldsymbol{g_{hkl} = hb_1 + kb_2 + lb_3}. \qquad (10)$$

The g_{hkl} vector is perpendicular to the hkl plane, while the distance between the planes (d_{hkl}) can be given as $2\pi/g_{hkl}$. The equation (11) is called the Bragg condition, which can be written as:

$$\boldsymbol{n\lambda = 2d_{hkl}sin\Theta} \tag{11}$$

where, θ is the half of the angle between k and k_0. The Bragg condition shows the relation of the λ_w wavelength, the d_{hkl} lattice parameter and angle of the incident wave to obtain an intensity maximum, Figure 3.19.

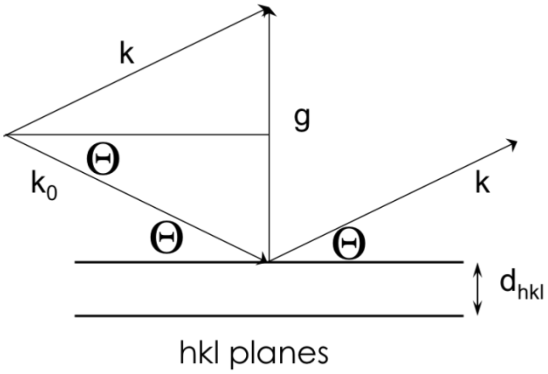

Figure 3.19: The Bragg condition

4 Materials and methods

The chapter deals with the materials investigated in this study, including the sample preparation and the experimental methods used in this study. The results are restricted to a representative sample for each condition.

4.1 Investigated materials

4.1.1 Pure Mg

Mg with a purity exceeding 99.99% produced by *Jiuli Magnesium Co. Ltd.* in China was used in the as-received and as-casted condition. Rods of 5 mm of diameter were prepared by machining and then cut to obtain samples of 10 mm in the lengths.

4.1.2 ZKQX6000 alloy

The ZKQX6000 (Mg- 6Zn-0.4Ag- 0.2-Ca- 0.6Zr (wt%)) (Mg-2.4Zn- 0.1Ag-0.1Ca-0.16Zr (at%)) alloy was produced at the *Magnesium Innovation Center* at the *Seoul National University*. The samples were prepared by electric melting of high-purity Zn, Mg, Ag, Ca and Mg-30 at.% Zr master alloy under a cover gas mixture of CO_2 and SF_6 in a steel crucible and casting them into a steel mould. Afterwards this the ingots were homogenized for 48 h at 350 °C with an Ar flow rate of 100 ml min^{-1}. The ZKQX6000 alloy was extruded at 350 °C with an extrusion ratio of 20 and a ram speed of 0.08 mm s^{-1}. Finally, the ZKQX6000 alloy samples were cut by electric discharge in rods of 5 mm and then cut into samples of 10 mm length.

4.2 Sample preparation

This section deals with the preparation of pure Mg and the ZKQX6000 alloy samples for light optical microscopy and texture measurements.

4.2.1 Preparation of pure Mg

Embedding: Samples were embedded in a multicomponent cold rubber (Demotec 30) with a mixture of methyl methacrylate powder and liquid.

Grinding: Pure Mg was ground with SiC-grinding discs with a granularity of 800, 1200 and 2500 using a Struers polishing machine. The final grinding step was done manually to avoid abrasive scratches. The first two grinding steps were carried out for 10 minutes each, while the last stage by manual grinding took about 30 minutes. The samples were washed and dried after each grinding step.

Polishing: The pure Mg samples were polished with an abrasive polishing cloth in combination with a water free 3 µm diamond paste (Struers) and a lubricant based on alcohol for 30 minutes. To remove narrow scratches and twins from the previous preparation step, the specimens were further polished with a Struers OP-Chem cloth with a colloidal silica solution (OP-S) with a particle size of 50 nm for up to 8 hours. After each step the samples were washed with ethanol and dried to remove surface debris and to prevent oxidation. The polishing procedure was finished by cleaning the samples with ethanol on a clean OP-Chem to remove traces of OP-S for 1 minute.

Etching: For optical microscopy the samples of pure magnesium were etched with a solution composition of:

30-40 ml distilled water

6.5-7 ml acetic acid (J.T. Barker)

140 ml ethanol

20 mg picric acid (Fluca Analytical)

After etching the samples were cleaned with ethanol.

Electro polishing (Preparation for EBSD): Even with a mechanical preparation time of up to 9 hours small scratches or twins remain due to the low hardness. Samples were polished with OP-S to remove the chemical etched surface. To reduce surface stresses produced during mechanical polishing, samples were electropolished with an Electropol-5 machine by Struers using a voltage of 33V and a flow rate of 9 for 90 seconds. The electrolyte AC2-I from Struers has following composition (Struers 2008) :

65-85 ml.	*Ethanol*
5-20 ml.	*Propan-1-oI*
<10 ml.	*Chinolin-8-oI*
<10 ml.	*Citric acid*
<5 ml.	*Water*

After electro polishing the samples were cleaned with a mixture of 5% nitric acid and ethanol to remove the oxide layer.

4.2.2 Preparation of ZKQX6000

Embedding: The embedding procedure was the same as with pure magnesium, see previous section.

Grinding: The ZKQX6000 alloy was grinded using SiC-paper with grit sizes of 500 to 2500 and all steps were done automatically for 8 minutes each.

Polishing: The polishing time was of to 2 hours per sample and was done with an OP-cloth in combination with a water free 1 µm diamond paste (Struers) and a lubricant based on alcohol. After polishing the samples were cleaned with ethanol on a clean OP-cloth.

Etching: Due to the smaller grain size, an etchant with a different chemical composition was used. With this etchant it is easier to highlight grain boundaries and to distinguish between them.

The composition of the etching solution was:

30 ml distillated water

20 ml acetic acid (J.T. Barker)

50 ml ethanol

60 ml ethylene glycol

1-2 ml nitric acid

10 mg picric acid (Fluca Analytical)

After etching the sample were polished back and cleaned again with ethanol.

4.3 Experimental techniques

4.3.1 Synchrotron X-Ray diffraction: *In situ* compression tests

In situ compression tests using synchrotron high energy X-ray diffraction was conducted at DESY (Deutsches Elektronen-Synchrotron) at the P07 (High Energy Materials Science) beamline – PetraIII. The beam used for characterisation was a monochromatic X-Ray beam with a beam energy of 100 keV (λ_W=0.124 nm) and a cross section of 1.0 mm x 1.0 mm. Diffraction patterns were recorded at a frame rate of about 3 per second using a PerkinElmer 1621 flat panel detector (200 μm^2) which was placed at a distance of 1745.6 mm from the specimen position. The acquisition time was 1.0 s. The sample-to-detector-distance was calculated using Fit2D software with a LaB6 sample. The specimen was mounted in the chamber of a dilatometer DIL 805A/D (Bähr-Thermoanalyse GmbH, Hüllhorst, Germany) with a modified heating induction coil so the beam passes through the sample, as shown in Figure 4.1. In the case of hot deformation, the temperature was controlled by a thermocouple type S, spot welded on the surface of the sample.

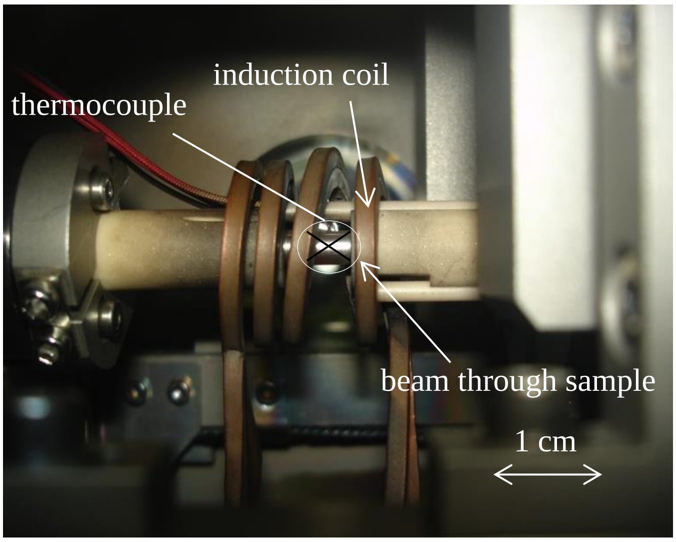

Figure 4.1: Setup for *in situ* compression tests at the P07 (HEMS) beamline at PETRA III

The specimens were heated to the tested temperatures up to 250°C at a rate of 30°C/s and held at the temperature for 3 min. Then, compression test was carried out at a constant anvil speed of 0.011 mm/s, meaning an initial mean strain rate of 1.1 x 10^{-3} s^{-1}. The tests were stopped after deformation up to 0.05, 0.1 and 0.3 of stress to evaluate deformation. The morphology of the Debye-Scherrer rings was then analysed using Fit2D software. Azimuthal-angle/time

(AT) plots were designed using ImageJ software package. Information about grain rotation, grain refinement, grain displacement and grain orientation was measured from these images.

Furthermore, the changes in intensities of the Debey-Scherrer rings were evaluated by plotting the 2θ-intensity curves using Fit2D. A macro was written, using MATLAB software to determine the maximum peaks in the 2θ-areas of interest over time, regarding to the diffracted planes. With the changes in intensities between coupled planes it was possible to draw conclusions about twinning.

4.3.2 Microstructure investigations - Light optical microscopy (LOM)

The LOM analysis was carried out on a Leica DMI500 M microscope. Magnifications of 1.6x and 10x for the pure Mg and 50x and 100x for the ZKQX6000 were used. The grain size was measured using analySIS Pro software. Five horizontal guide lines parallel to the extrusion direction on the measured area were taken in consideration and crossing grain boundaries were selected manually on these lines. The average grain size was then computed via statistic distribution automatically.

4.3.3 Microstructure investigations - EBSD

The Electron Backscatter Diffraction (EBSD), also known as Backscatter Kikuchi Diffraction (BKD), is a Scanning Electron Microscopy (SEM) based microstructural- crystallographic technique to measure the crystallographic orientation. This potent tool for microstructural characterisation can be used to index or rather identify the seven crystal systems and can be applied to measure crystal orientation, grain size, global texture, strain analysis. (Oxford Instruments 2013)

At the present research EBSD studies were carried out on a FEG-SEM Zeiss Ultra 55 scanning electron microscope. The maximum magnification of this device is x1.000.000 with nominal resolutions of 0.8 nm (at 30kV), 0.8 nm (at 15 kV) and 1.6 nm (at 1 kV). The system is assisted by a 5 axes (x,y,z,tran.,rot.) sample stage, a Hikari-Camera for EBSD and two EDX (Energy Dispersive X-Ray) detectors (SiLi and Apollo-SDD). The samples were tested in a vacuum chamber with a working distance of 13 mm between specimen and camera. For the ZKQX6000 alloy an area of 80 x 80 µm with a step size of 0.08 pixels and for the pure Mg an area of 400 x 400 µm with a step size of 0.8 pixels was investigated.

The Orientation Imaging Microscopy (OIM) Data Analysis software was used to evaluate the data for automated EBSD analysis. The OIM Data Analysis software is a powerful tool for data acquirement, orientation mapping and texture investigation.

The following OIM analysis tools have been used:

- Inverse pole figure (IPF)

  An inverse pole figure illustrates a two-dimensional representation of crystal orientation. With this tool it is possible to distinguish high angle from low angle boundaries. Each colour represents a defined crystallographic plane orientation with respect to a reference.

- Grain Reference Orientation Deviation (GROD)

  The GROD pictures the deviation of each point in the grain with respect to zhe average orientation within a grain. This tool is useful to identify sub-grain formation and high misoriented zones. In this work angles between 0° and 50° have been chosen.

- Kernel average misorientation (KAM)

  In the Kernel maps the average misorientation between a given data point and all of its neighbours (1^{st},2^{nd},3^{rd}, etc…) is calculated. In this work the 5 nearest neighbours are considered. With the Kernel average misorientation it is possible to evaluate the local misorientation especially close to grain boundaries.

- Gray scale map

  The gray scale maps show the quality of the EBSD pattern. In this work the qualities of the detector signal were used, providing a good background to picture e.g. twins in the microstructure.

5 Results

In this chapter the results from the synchrotron, LOM and the EBSD analysis of the pure Mg and the ZKQX6000 alloy are presented. An overview of the initial and final dimensions of the samples can be found in the Appendix I.

5.1 Metallography of as-received samples

5.1.1 Pure Mg

Figure 5.1 shows the microstructure of the as-received pure Mg sample at both low and high magnification. The measured average grain size was 1193±25 µm, Figure 5.1 a). The volume fraction of twins observed in the un-deformed pure Mg is attributed to the mechanical polishing. Regarding Figure 5.1a), it is observed that twins are confined to the edge of the sample rather than to the centre. There is no evidence of grain boundary particles in Figure 5.1 b). In the following images of microstructures the loading direction (LD), the same direction of extrusion, and the transverse direction (TD) are illustrated.

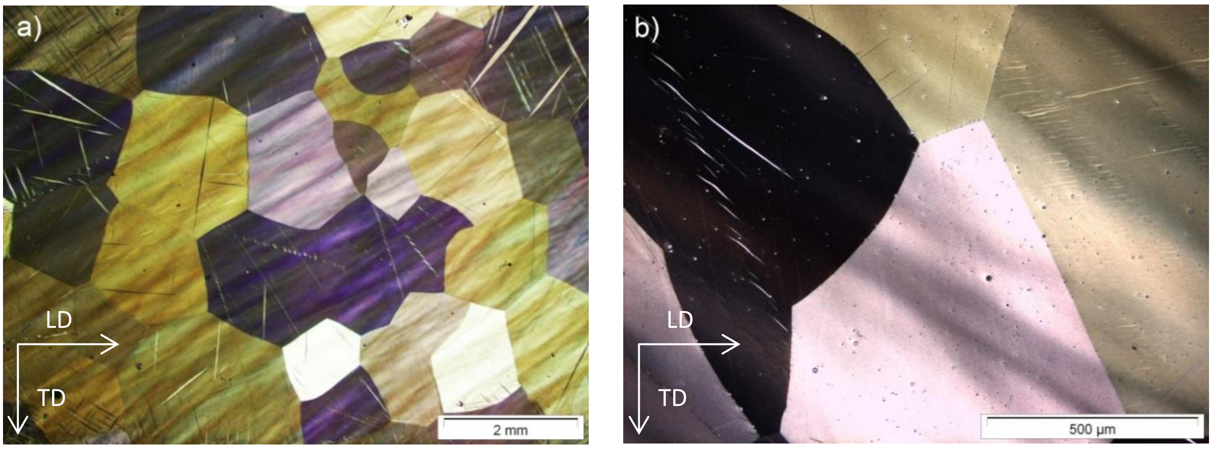

Figure 5.1: Light optical micrographs of as-received pure Mg with a) low magnification (1.6x) and b) high magnification (10x)

Figure 5.2 shows the EBSD inverse pole figures of the un-deformed Mg sample. In this detail, it is possible to observe a triple grain boundary. The black spots in the microstructure result from a surface contamination. It was not possible to evaluate the grain size due to the relatively small area investigated.

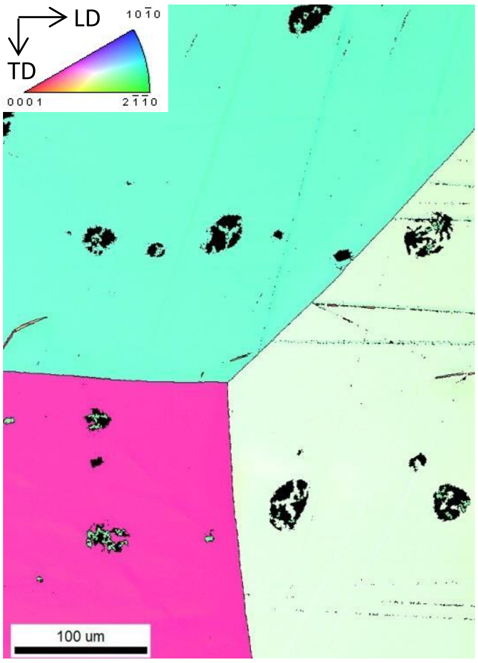

Figure 5.2: EBSD IPF maps showing a triple boundary in the as-received pure Mg

5.1.2 ZKQX6000 alloy

Figure 5.3 shows average grain size of the ZKQX6000 alloy in the as-extruded condition obtained from the light optical investigations was 6.9±1 µm. Mg (ZnZr) precipitates are located in high particle density bands (Mendis et al. 2009). No twins are observed in the as-extruded ZQKX6000 alloy. The light optical microscope image shows a heterogeneous distribution of the gain size. Finer grains are observed close to the intermetallic particles.

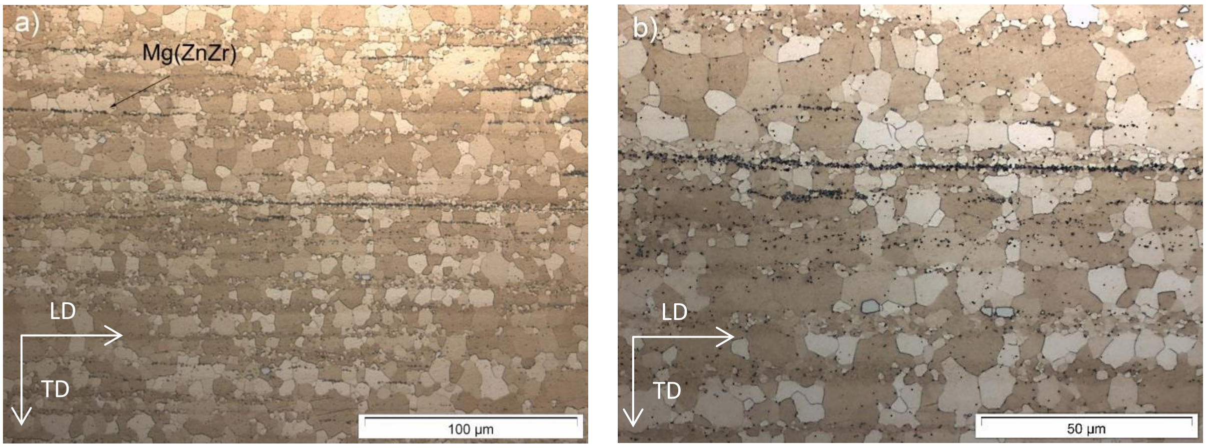

Figure 5.3: Light optical micrographs of as-extruded ZKQX6000 alloy with a) low magnification (50x) and b) high magnification (100x)

The IPF of the undeformed ZQKX600 sample is shown in Figure 5.4. The average grain size was determined using OIM software (tolerance angle = 5°) to be 7.1±0.5. The area investigated includes the characteristical fine grain regions parallel to the extrusion direction (LD).

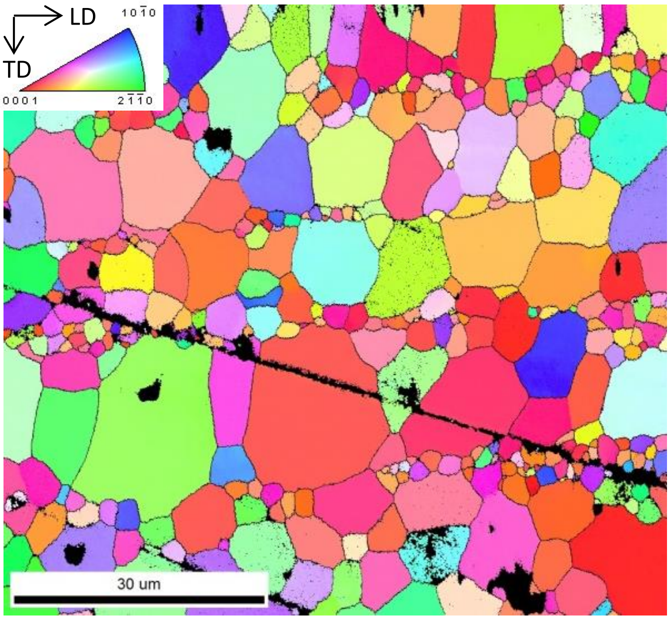

Figure 5.4: EBSD IPF maps showing the orientation of grains in the as-extruded ZKQX6000 alloy

5.2 Stress-strain curves in compression

5.2.1 Pure Mg

The compression stress-strain curves for pure Mg are shown in Figure 5.5. The RT test in compression to 0.05 of strain shows a yield stress at 0.02 of strain ($\sigma_{0.2}$) of approximately 20 MPa and the curve shows a change in slope after yielding.

The sample compressed to 0.1 of strain has a maximum stress of 83 MPa. The sample experiences a strengthening effect due to an inflection after yielding.

The sample deformed to a strain of 0.3 at RT shows a $\sigma_{0.2}$ of approximately 20 MPa again and a peak stress of 130 MPa. The change of the slope of the flow curve can be observed in detail between 0.02 and 0.05 of strain.

At 250°C, with 0.05 of strain a $\sigma_{0.2}$ of 10 MPa was observed. The flow curve shows a change in the slope at around 0.01 of strain. A stress value of 18 MPa was reached at a deformation of 0.05 of strain.

The sample deformed to 0.1 of strain has a maximum stress of 28 MPa. The sample shows work hardening after yielding.

Deformation to 0.3 of strain shows a $\sigma_{0.2}$ of approximately 10 MPa and a maximum stress of 50 MPa. Associated work hardening was observed after yielding. At approximately 0.1 of strain until the end of the compression test, a fluctuation of the flow curve was detected.

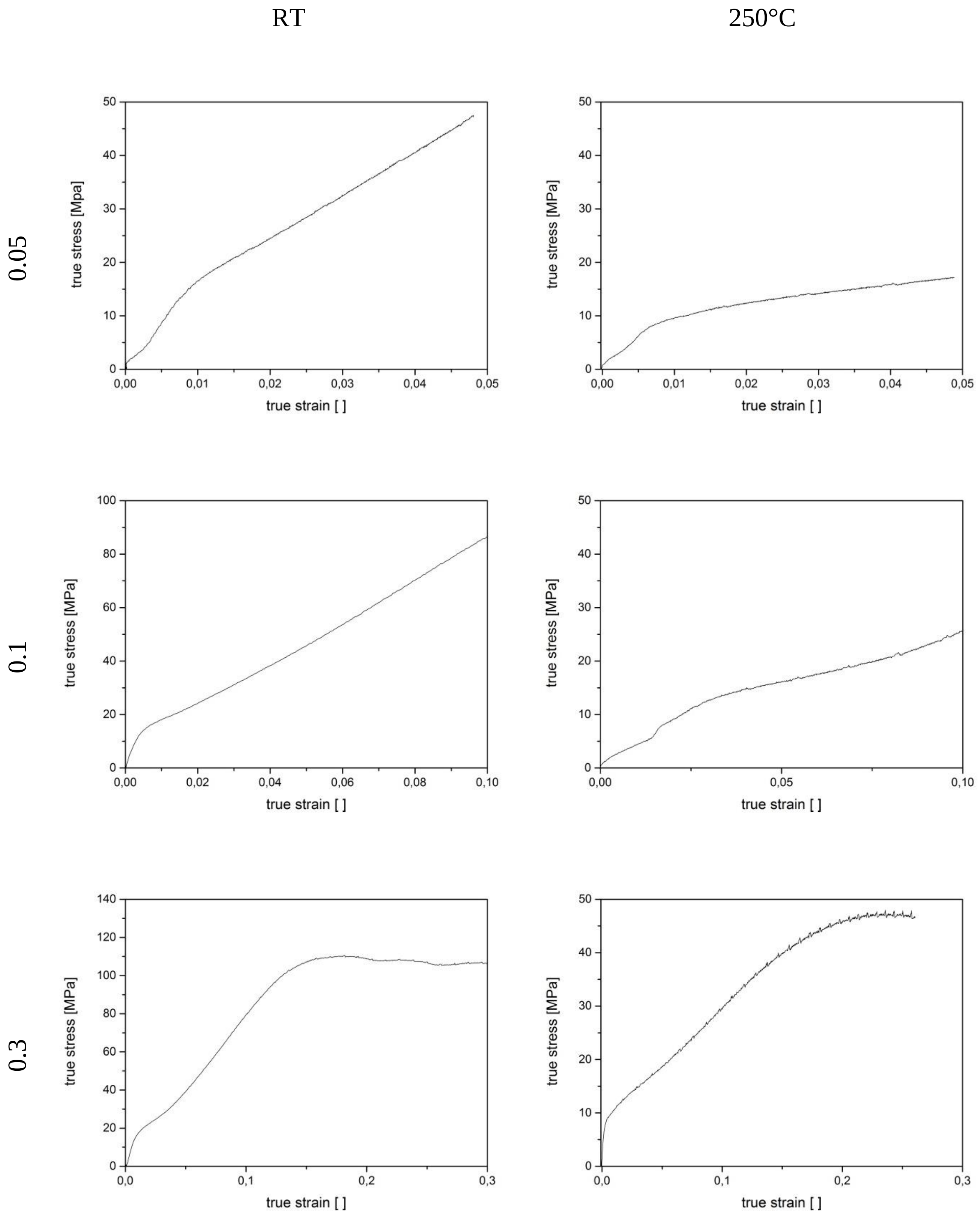

Figure 5.5: Stress-strain curves for compression of pure Mg

5.2.2 ZKQX6000 alloy

Figure 5.6 shows the stress-strain curves of the ZKQX6000 alloy. At RT, after deformation to 0.05 of strain it was observed that the sample shows work hardening after yielding, marked by a change in the slope. The maximum yield stress was detected at 210 MPa and the maximum stress at 220 MPa.

After deformation to 0.1 of strain a yield stress of 200 MPa and a maximum stress of 310 MPa was measured. Between 0.02 and 0.1 of strain work hardening was observed, marked by the appearance of a change in the slope.

At a deformation to 0.2 of strain a yield strength of 210 MPa was observed. The sample broke before reaching the desired strain of 0.3. A maximum strength of 410 MPa occurs at a strain of 0.2.

At 250°C, after a deformation of 0.05 of strain, a yield stress of 42 MPa was measured. After yielding no point of inflection was detected.

For the samples compressed to 0.1 and 0.3 strain, strain hardening was followed by steady state or slightly softening when the strain was larger than 0.02.

In general it can be seen that at 250°C at low strain rates the stress increases significantly and softening occurs after reaching a maximum strength of 48 MPa.

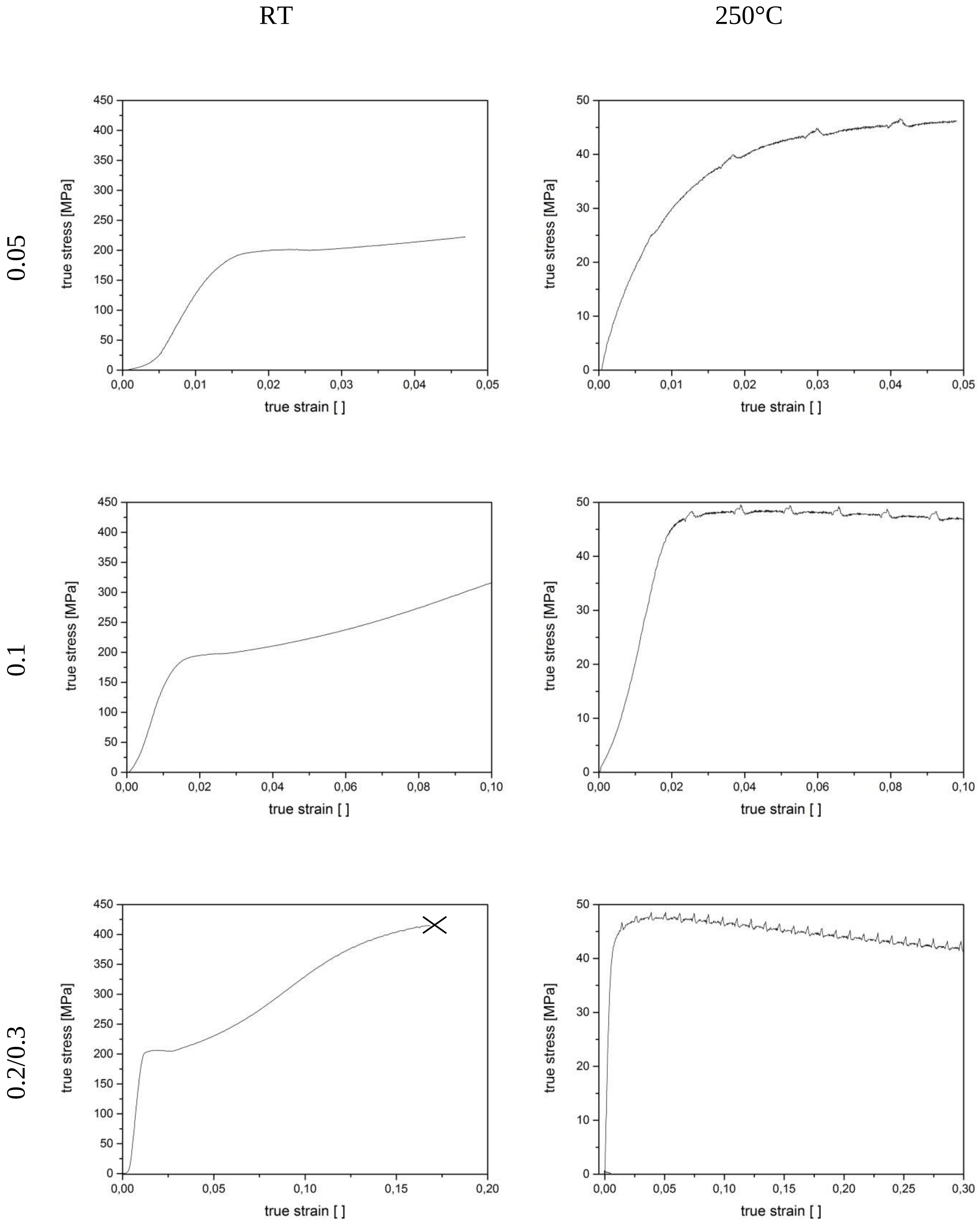

Figure 5.6: Stress-strain curves for compression of ZKQX6000 alloy

5.3 *In situ* synchrotron diffraction

In this section the results from the *in situ* synchrotron diffraction experiments are presented. In the first part the intensity changes of coupled pairs of planes are shown by increasing the strain. In Mg there are two important pairs of diffraction lines which are coupled and their changes in intensity indicate twinning, marked by a simultaneous increase and decrease of intensity. These pairs of planes are the (0002)-basal-$\{10\bar{1}0\}$-prismatic and the $\{11\bar{2}0\}$-prismatic–$\{10\bar{1}3\}$-pyramidal 3rd order, both related to tensile twinning. Additionally, A-T plots for 0.3 of strain at RT and 250°C are presented.

5.3.1 Pure Mg

Intensity changes

The changes of the maximum value for selected diffraction lines of the integrated line profiles during deformation of pure Mg at RT and 250°C are shown Figure 5.7.

Pure Mg deformed at RT shows an early change of intensity between the (0002)–$\{10\bar{1}0\}$ peaks. The intensity of the (0002) peak for the sample deformed to 0.05 of strain decrease until a strain of 0.025, where an intersection with the increased intensity of the $\{10\bar{1}0\}$ peaks is observed (Figure 5.7 a)). This was also observed in the sample deformed to 0.3 of strain. In both cases, no change in intensities was observed after a strain of 0.025 (Figure 5.7 c)). But the sample deformed to 0.1 of strain, shows an intensity change between 0.03 and 0.08 of strain, shown in Figure 5.7 c). Furthermore, no changes in intensity at RT were observed between $\{11\bar{2}0\}$–$\{10\bar{1}3\}$ plane pairs.

No mentionable intensity changes were observed at the sample compressed at 250°C to 0.05 of strain, shown in Figure 5.7 d). With advanced deformation a change of intensities between the (0002) – $\{10\bar{1}0\}$ peaks becomes apparent. The change was detected at approximately 0.03 strain in the sample compressed to 0.3 strain, illustrated in Figure 5.7 e). Also at temperatures of 250°C no change in the $\{11\bar{2}0\}$–$\{10\bar{1}3\}$ peaks were noticed.

The integrated line profiles (2θ-intensity curves) for all deformation conditions at RT and 250°C are shown in the Appendix II.

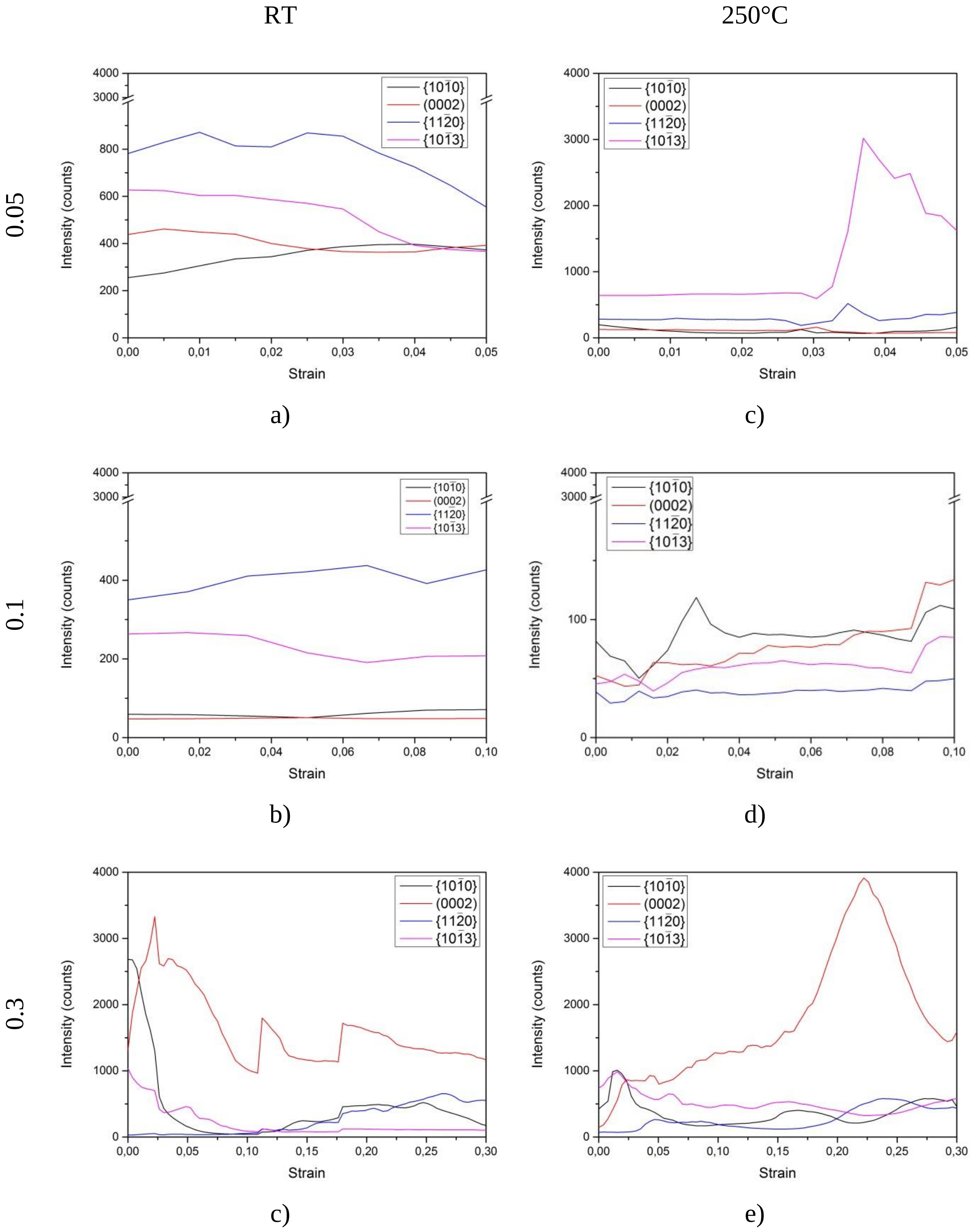

a) c)

b) d)

c) e)

Figure 5.7: The changes in the peak intensities of selected diffraction lines of the integrated line profiles during deformation of pure Mg at RT and 250°C

A-T plots

The A-T plots of the pure Mg sample deformed at RT up to 0.3 of strain are shown in Figure 5.8. Before compression starts, discrete lines corresponding to individual grains were observed. When compression starts (see flow curves on the right) these lines start to bend (see red arrows). With ongoing compression the diffraction lines begin to broaden or blur (see green arrows), Figure 5.8. The yellow arrows demonstrate the splitting of diffraction lines during compression.

Figure 5.9 shows that in the beginning of compression of the pure Mg at 250°C some diffraction lines experience a bending (see red arrows), followed by a broadening (see green arrows). With continued compression a mosaic spread of the diffracted lines was observed (see orange circles).

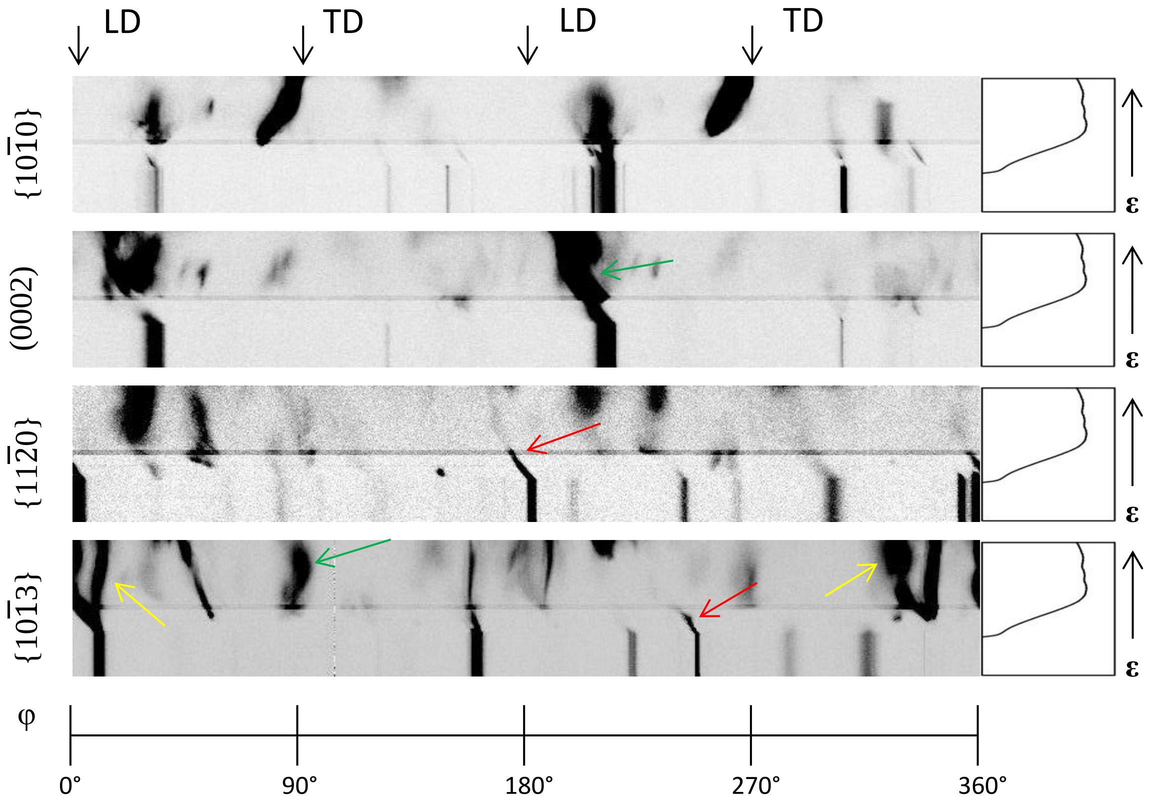

Figure 5.8: A-T plots of pure Mg at RT during compression up to 0.3 of strain

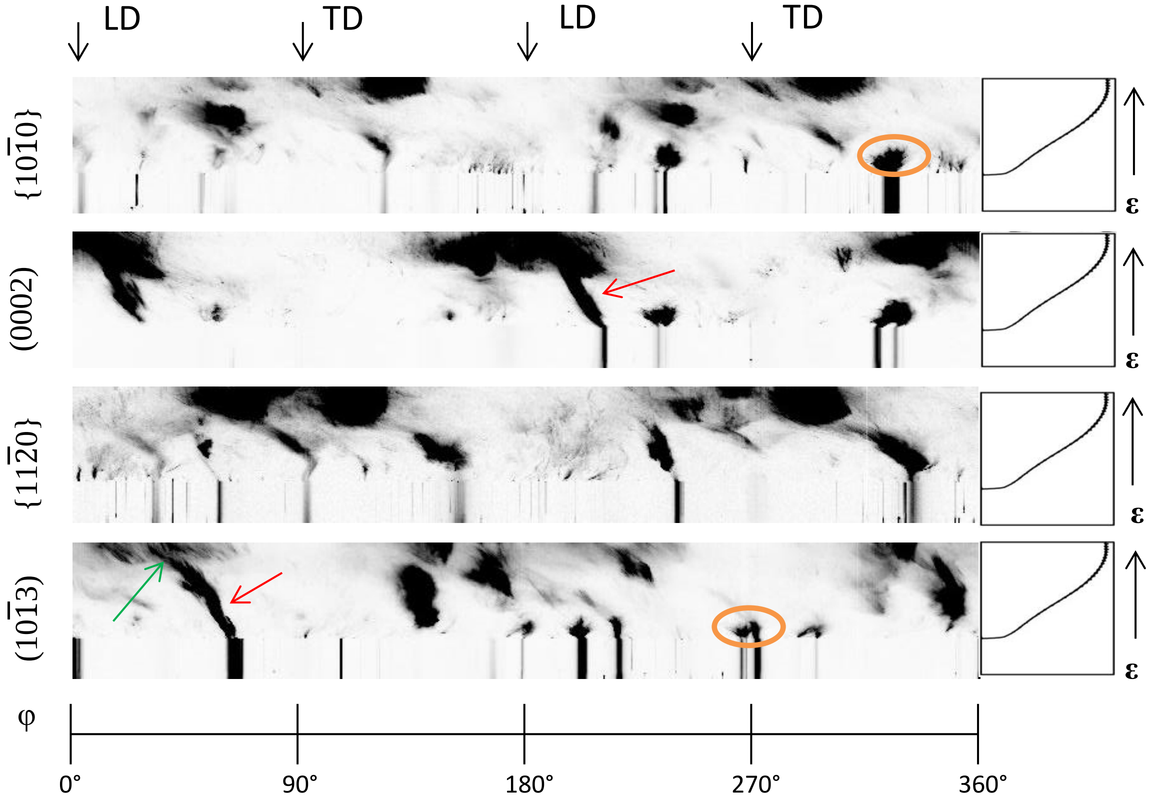

Figure 5.9: A-T plots of pure Mg at 250°C during compression up to 0.3 of strain

5.3.2 ZKQX6000 alloy

Intensity changes

The changes of the maximum intensities in between selected 2θ areas for the ZKQX6000 alloy are shown in Figure 5.10.

Figure 5.10 shows that the intensity for the (0002) planes increases continuously from 0.025 of strain, while a decrease of the {10$\bar{1}$0} planes was observed. No change in intensities for {11$\bar{2}$0}–{10$\bar{1}$3} planes for all deformation condition was detected, illustrated in Figure 5.10 a), b) and c).

During compression at 250°C the intensity peaks do not show a significant change (Figure 5.10 c), d)). Only some slightly changes in the (0002)–{10$\bar{1}$0} planes and the {11$\bar{2}$0}–{10$\bar{1}$3} planes for the sample compressed to 0.3 strain were observed (Figure 5.10 e)).

The integrated line profiles (2θ-intensity curves) for all deformation conditions are shown in the Appendix II.

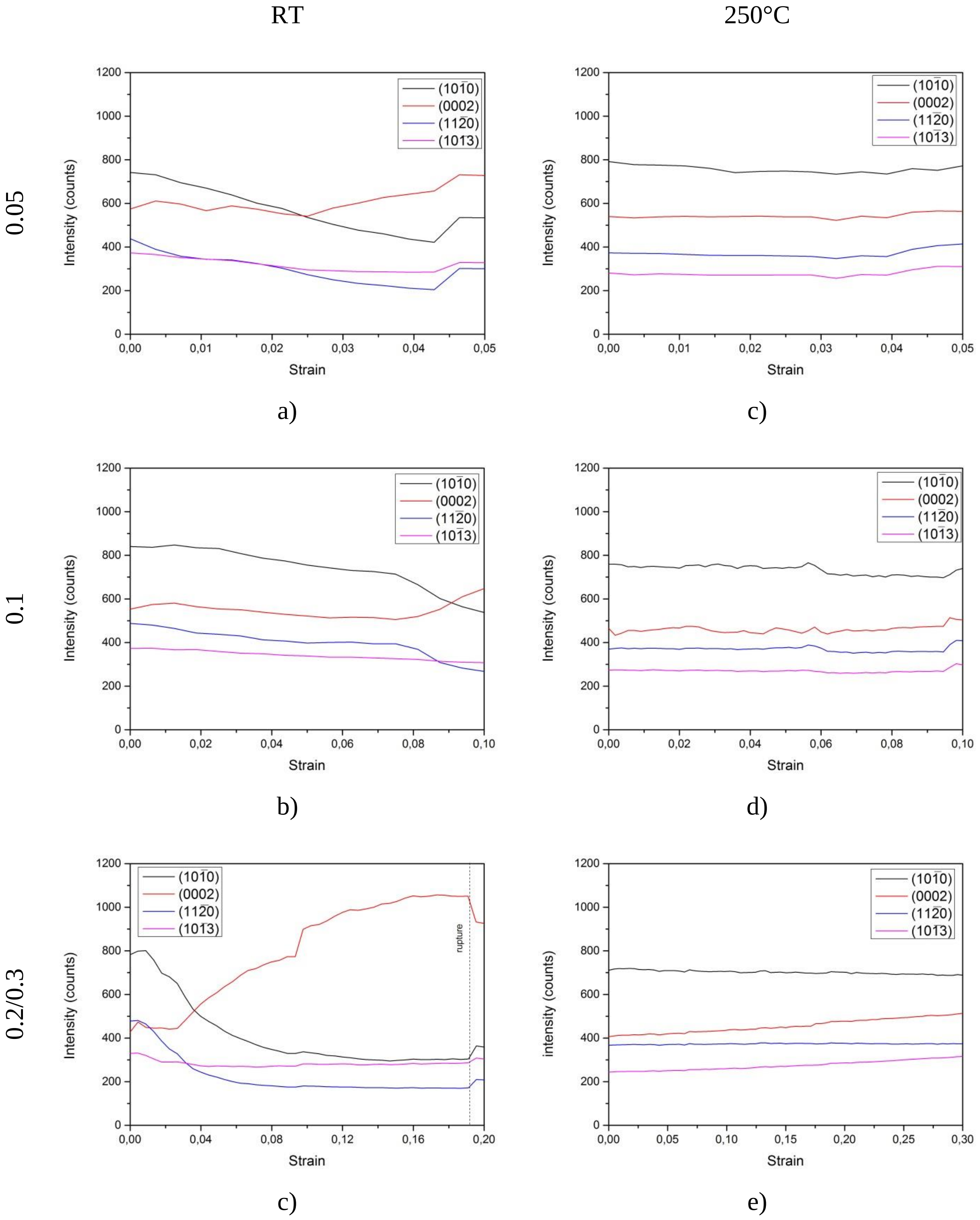

a) c)

b) d)

c) e)

Figure 5.10: The changes in the peak intensity of selected diffraction lines from the integrated line profiles during deformation of the ZKQX6000 alloy at RT and 250°C

A-T plots

The A-T plots of the ZKQX6000 alloy compressed at RT up to 0.3 of strain, are shown in

Figure 5.11. Before compression starts the grains appear as narrow lines. These lines experience a small shift in φ-direction when compression is initiated. With continued deformation the diffracted lines blur and no bending was observed. Initial preferred orientation is replaced for a new preferred crystal orientation on the deformed material.

Figure 5.12 illustrates the deformation of ZKQX6000 alloy at 250°C. As the compression starts, a bending of some diffraction lines is observed (see red arrow). These lines start to broaden before blurring (see blue arrow) with ongoing compression. This process can be seen clear along the LD in (0002). At higher compression strains, the diffraction lines blur completely and cones are formed (see green lines). Contrary to the RT deformation test shown in Figure 5.11, preferred original crystal orientation is intensified during deformation.

It is worth to note, that the final crystal preferred orientation are similar after deformation at RT as well as at 250°C.

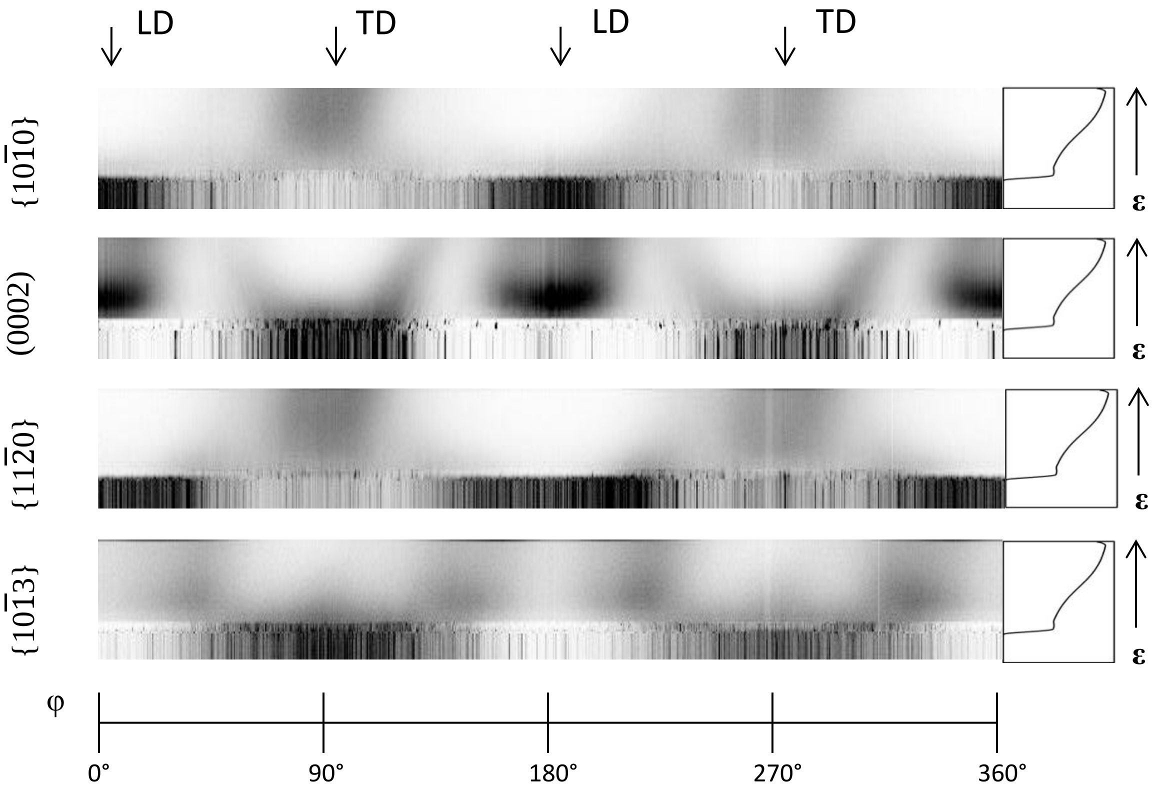

Figure 5.11: A-T plots for ZKQX6000 alloy at RT during compression up to 0.3 of strain

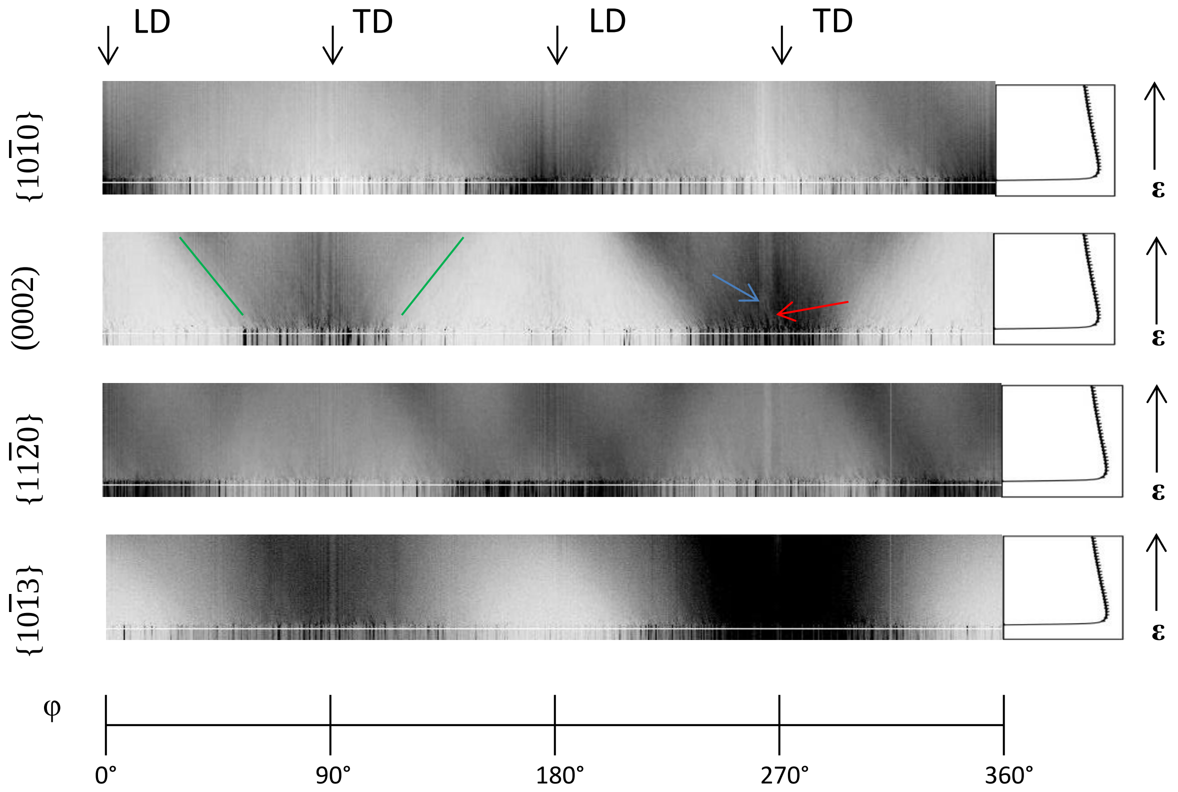

Figure 5.12: A-T plots for ZKQX6000 alloy at 250°C during compression up to 0.3 of strain

5.4 Examination of deformed microstructure – LOM

5.4.1 Pure Mg

At RT:

Figure 5.13 shows the microstructure of pure Mg after deformation at RT to a strain of 0.05. Deformation twins are observed in Figure 5.13 a).

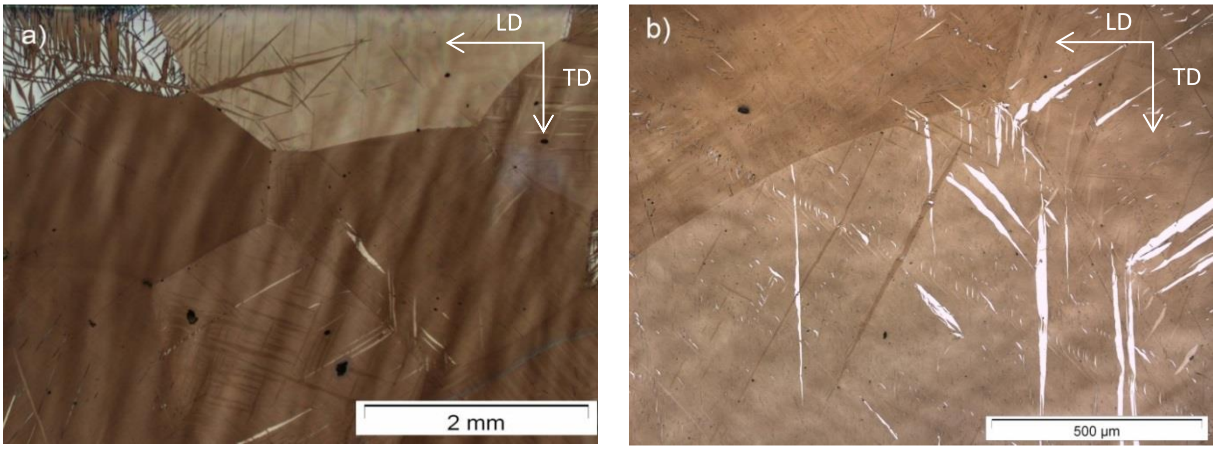

Figure 5.13: Light optical micrographs of pure Mg compressed up to 0.05 of strain at RT

Unfortunately it was not possible to estimate the average grain size of this sample using standard metallographic methods, due to the dimension of the grains and the small surface of the prepared sample. In Figure 5.13 b) with a magnification of 10x typical twins at three grains are shown.

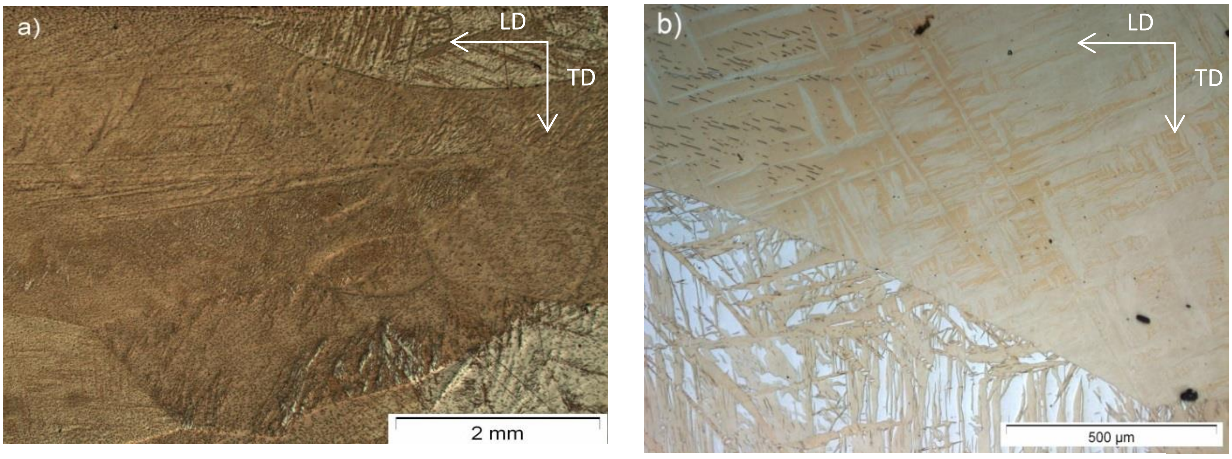

Figure 5.14: Light optical micrographs of pure Mg compressed up to 0.1 of strain at RT

The volume fraction of twins increases by increasing the strain up to 0.1, as shown in Figure 5.14.

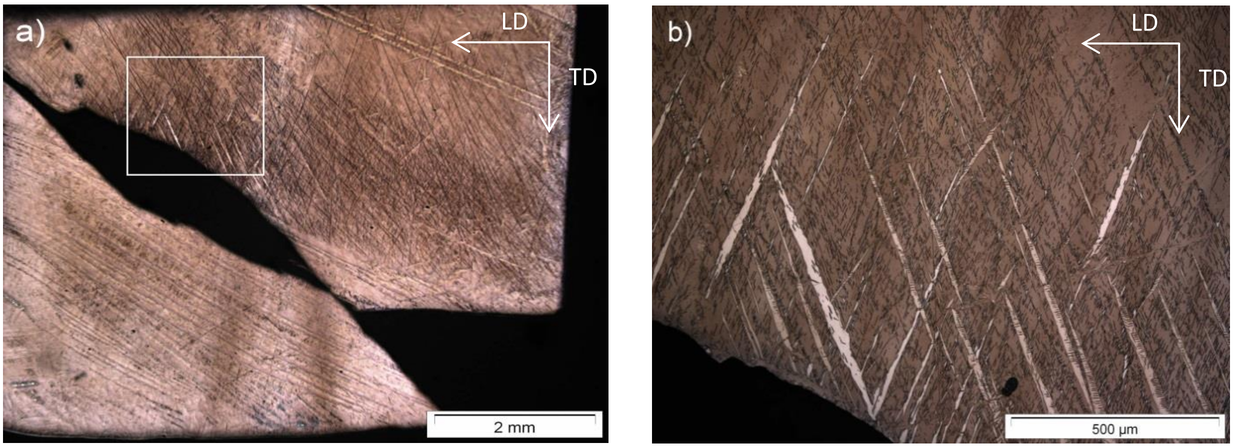

Figure 5.15: Light optical micrographs of pure Mg compressed up to 0.3 of strain at RT

Figure 5.15 a) shows the broken pure Mg specimen deformed up to 0.3 strain at RT. The sample is broken in a 45° angle to the loading direction. A high fraction of twins on the fracture region was observed, as shown in detail in Figure 5.15 b).

At 250° C:

Figure 5.16 illustrates pure Mg compressed to 0.05 of strain at 250°C. The volume fraction of twins is low, but it can be observed that these twins show a wide base. It can be additionally observed, that twins are preferentially formed in some grains.

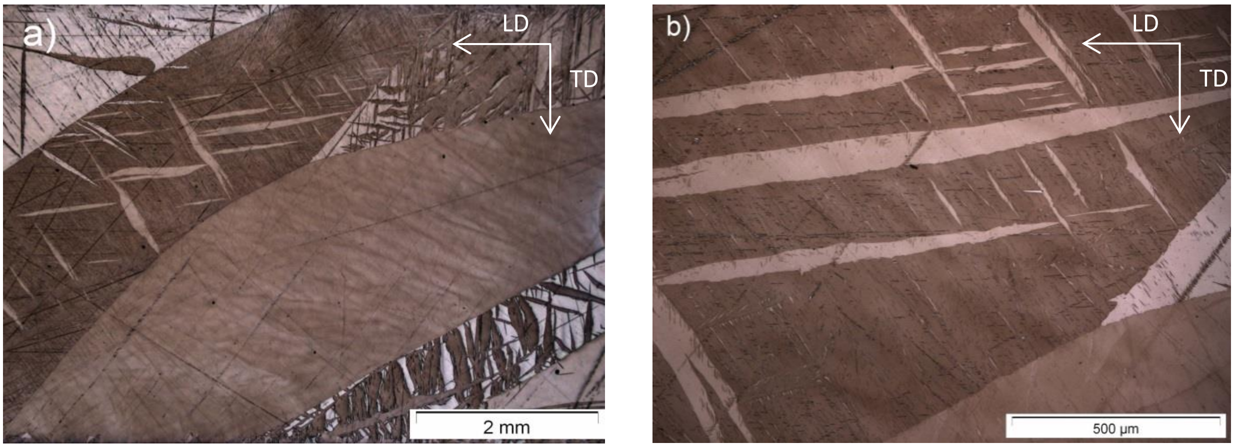

Figure 5.16: Light optical micrographs of pure Mg compressed up to 0.05 of strain at 250°

After a deformation up to 0.1 strain, the sample shows a lower density of twins, than if deformed up to 0.05 of strain, shown in Figure 5.17. Furthermore, grain boundary serrations are observed.

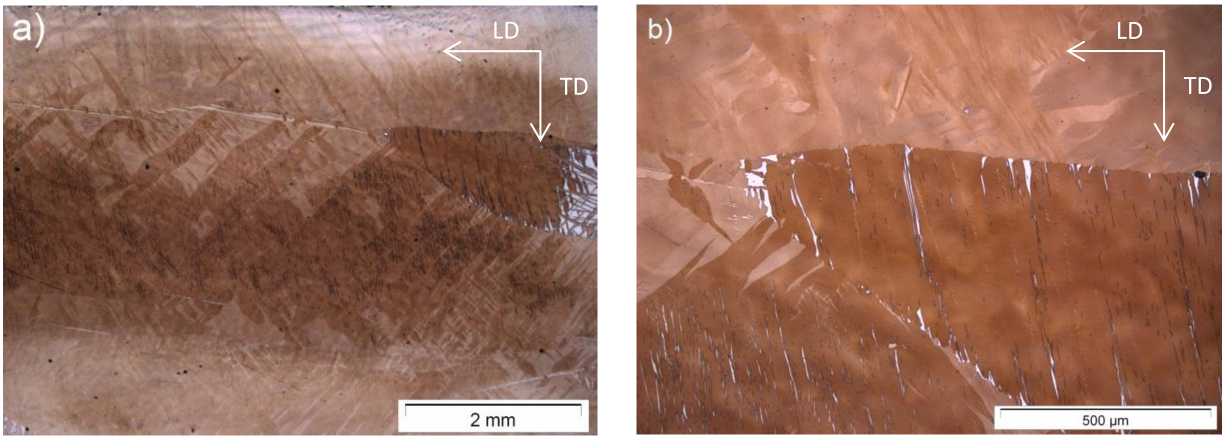

Figure 5.17: Light optical micrographs of pure Mg compressed up to 0.1 of strain at 250°C

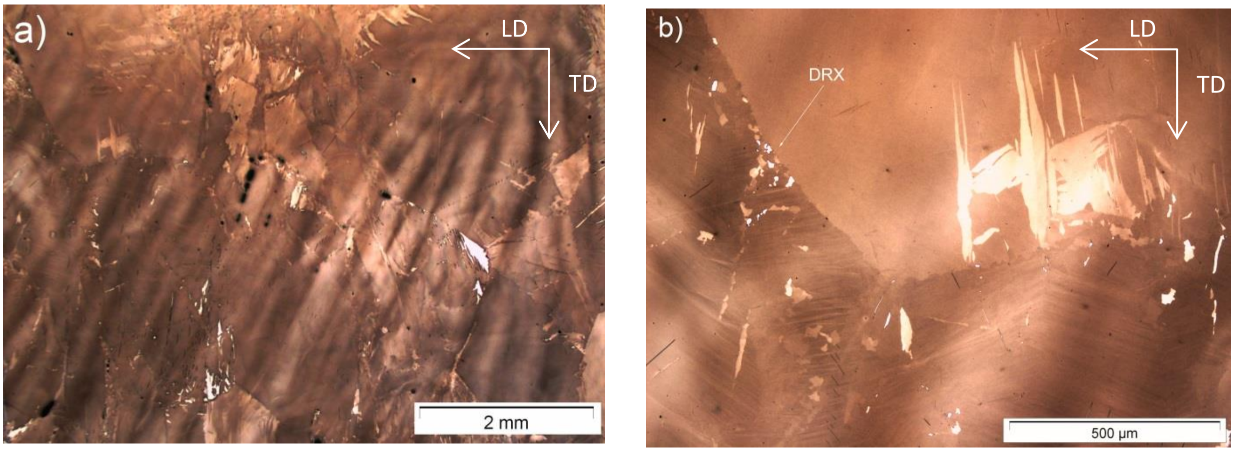

Figure 5.18: Light optical micrographs of pure Mg compressed up to 0.3 strain at 250°C

The Figure 5.18 a) shows the microstructures of the sample deformed up to 0.3 of strain with smaller grain size in some regions, though the grain boundaries are harder to identify. The sample exhibit a smaller amount of twins compared to the previous strain conditions. A detail of fine grains is observed in Figure 5.18 b) and Figure 5.19.

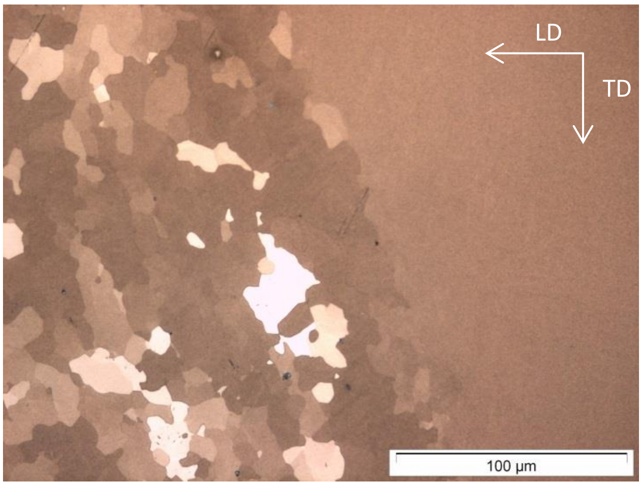

Figure 5.19: Formation of small grains in pure Mg at a deformation up to 0.3 of strain and 250°C

5.4.2 ZKQX6000 alloy

At RT:

The micrograph of the sample deformed at RT up to 0.5 of strain is shown in Figure 5.20. Twins are formed heterogeneously during cold deformation, shown in Figure 5.20 b).

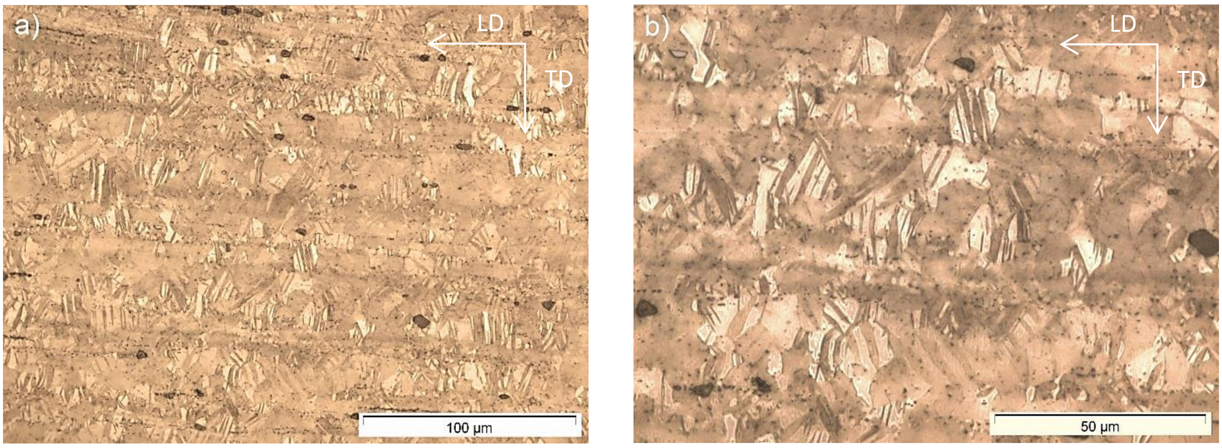

Figure 5.20: Light optical micrographs of ZKQX6000 alloy compressed up to 0.05 of strain at RT

After a deformation up to 0.1 of strain the sample shows a constant or even lower area fraction of twins, shown in Figure 5.21. Figure 5.21 b) illustrates grains containing narrow twins.

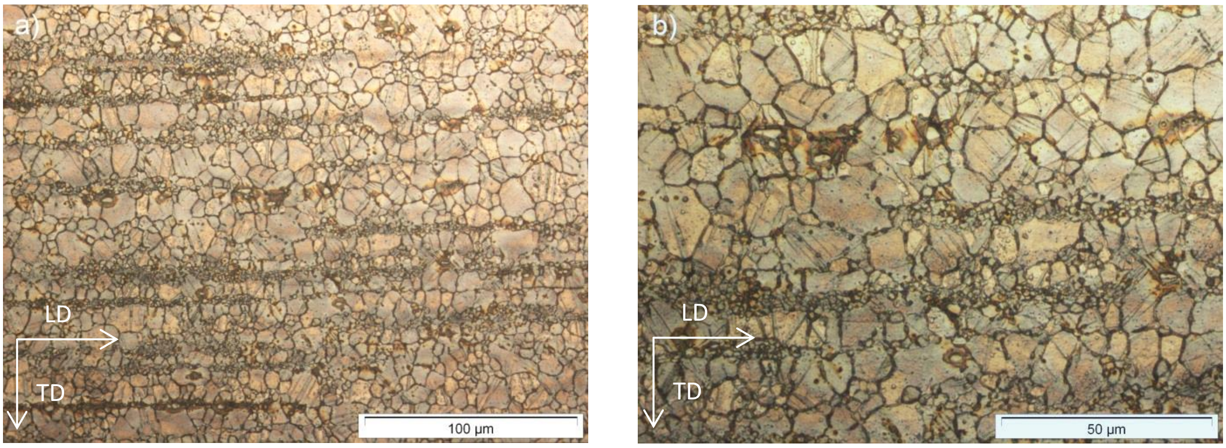

Figure 5.21: Light optical micrographs of ZKQX6000 alloy compressed up to 0.1 of strain at RT

Figure 5.22 shows the microstructure of the sample compressed up to 0.2 of strain (fracture) at RT. With increased strain the volume of twins decreases or stays relatively constant, see Figure 5.22 b). It reveals that many grains are occupied by deformation twins.

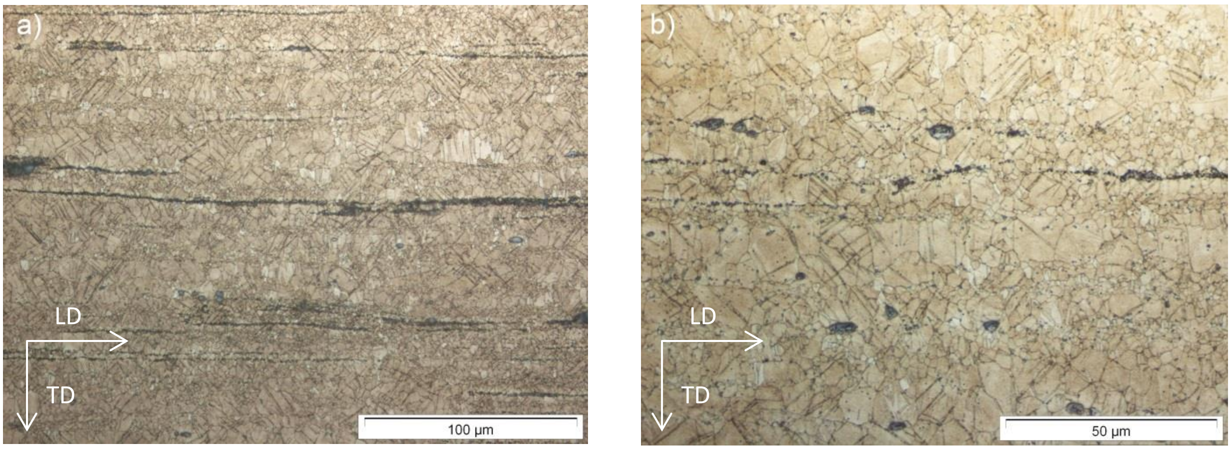

Figure 5.22: Light optical micrographs of ZKQX6000 alloy compressed up to 0.2 of strain at RT

At 250° C:

After a deformation at 250°C up to 0.05 of strain, a grain size of 6.0±0.8 µm was measured and no twins were observed in the microstructure (Figure 5.23 b). The block spots on the microstructure represent artefacts, due to the preparation.

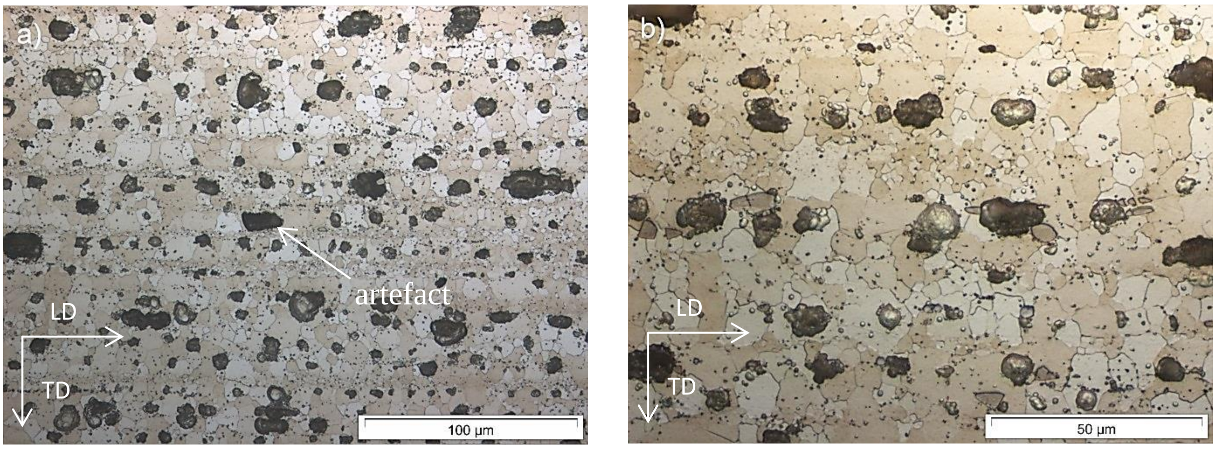

Figure 5.23: Light optical micrographs of ZKQX6000 alloy compressed up to 0.05 of strain at 250°C

Figure 5.24 shows the microstructure of the sample deformed up to 0.1 of strain. An accumulation of smaller grains is observed at the grain boundaries, in addition to the initial bands of intermetallic particles. Twins were not observed and a grain size of 4.8± 0.5 µm was measured. Furthermore, grain boundary serration occurred.

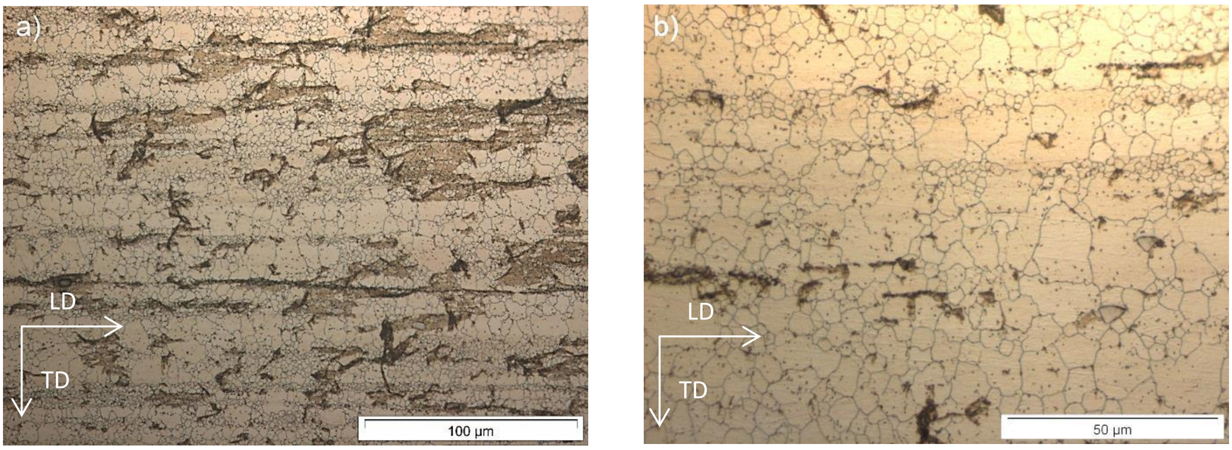

Figure 5.24: Light optical micrographs of ZKQX6000 alloy compressed up to 0.1 of strain at 250°C

The microstructure of the sample deformed up to 0.3 of strain, in Figure 5.25, shows an average grain size of 3.0±0.7 µm. The black spots on the surface are related to intermetallics or artefacts. A high volume of small grains are distributed at grain boundaries. Twins were not observed.

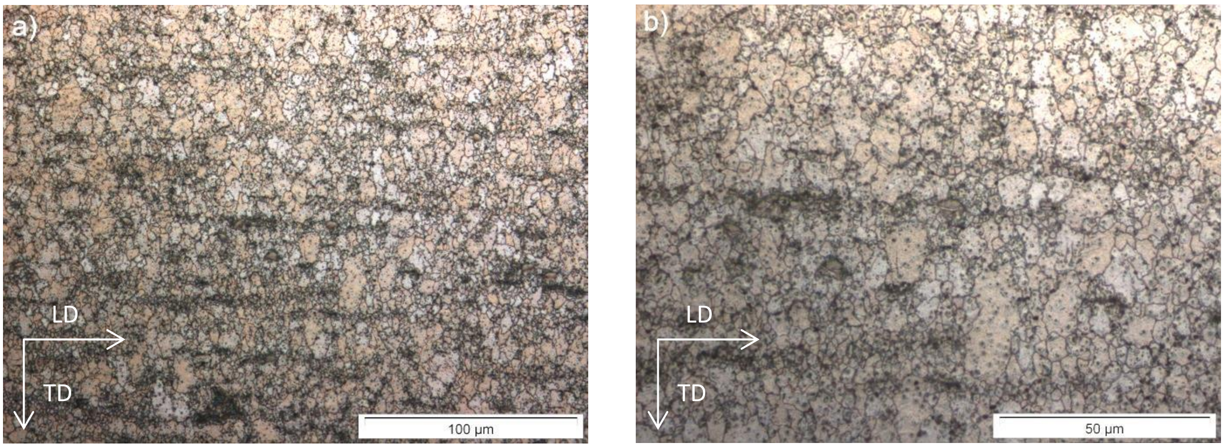

Figure 5.25: Light optical micrographs of ZKQX6000 alloy compressed up to 0.1 of strain at 250°C including artefacts

5.5 Examination of deformed microstructure - EBSD

This section deals with the investigation of the microstructure of the samples after deformation by means of EBSD analysis.

5.5.1 Deformation of pure Mg

Figure 5.26 shows the IPF maps of pure Mg after deformation at RT and 250°C. Only a small area of the samples was investigated with reference to the grain size. In the detailed pictures, twin formation and recrystallized grains were observed at RT and 250°C, respectively. Additionally, gray scale maps are shown in Figure 5.27 to highlight twin formations.

Representatively, shows the data set of the sample deformed at RT up to 0.05 of strain. Each twin boundary is marked with a representative colour, direction and angle. The area fraction gives information about the volume of twins in the investigated area.

Table 5.1: Data set of twinning for pure Mg at RT and 0.05 of strain

Boundaries: Twin (Axis-Angle with K1 Plane)						
	K1 Plane	Direction	Angle	Type of twin	Tolerance	Area Fraction
------	$\{11\bar{2}0)$	$<11\bar{2}0>$	86.3°	tensile	5°	0.175
------	$\{10\bar{1}1\}$-$\{10\bar{1}2\}$		37°	double	5°	0.000
------	$\{10\bar{1}1\}$	$<11\bar{2}0>$	56.2°	compression	5°	0.000
Boundaries: Grain						

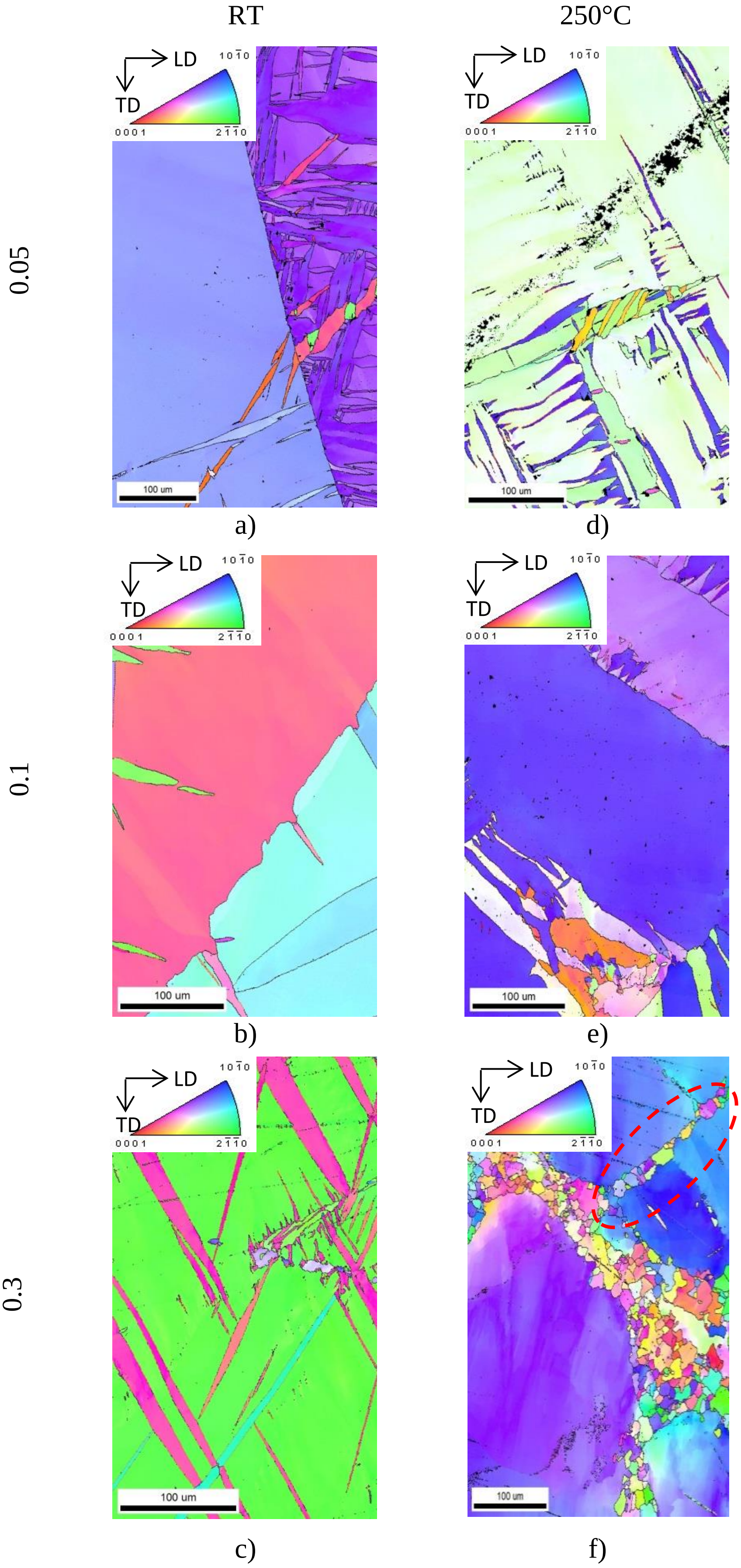

Figure 5.26: IPF map of pure Mg showing grain boundaries and twins up to a) 0.5 b) 0.1 c) 0.3 of strain at RT and d) 0.5 e) 0.1 f) 0.3 of strain at 250°C

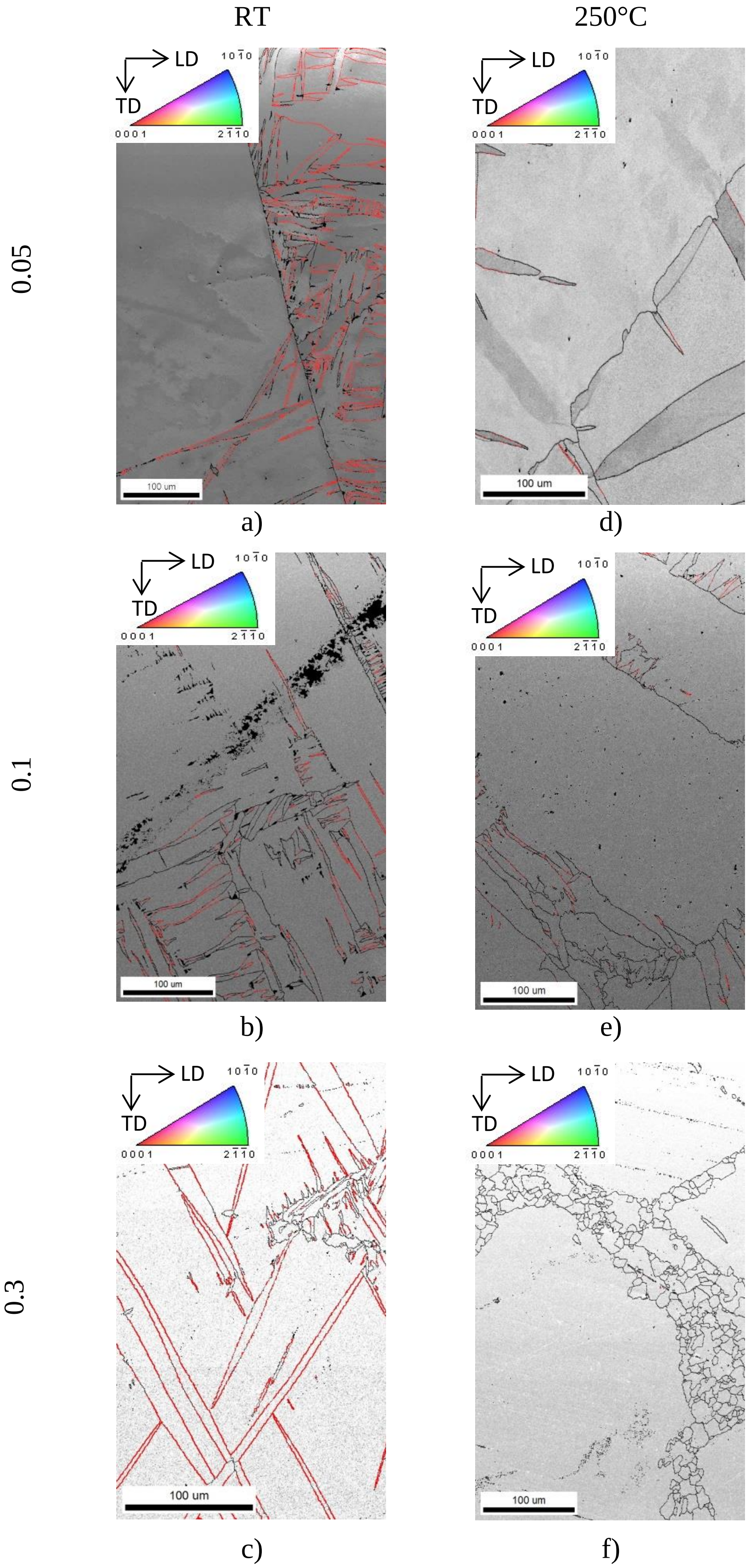

Figure 5.27: Gray scale maps of pure Mg showing grain boundaries and twins up to a) 0.5 b) 0.1 c) 0.3 of strain at RT and d) 0.5 e) 0.1 f) 0.3 of strain at 250°C

In all samples exclusively {11$\bar{2}$0} <11$\bar{2}$0> tensile twins were found. At RT the sample deformed up to 0.05 of strain shows tensile twins with an area fraction of 0.175, shown in Figure 5.27 a). The sample deformed up to 0.3 of strain shows a higher volume of tensile twins with an area fraction of 0.304, shown in Figure 5.27 c). It is noted that at 0.1 of strain the highest fraction of tensile twins with a value of 0.544 was observed (Figure 5.27 b))

At 250°C, after deformation up to 0.05 of strain the tensile twins have an area fraction of 0.139 (Figure 5.27 d)), which is lower than that at RT. After deforming to 0.1 of strain an area fraction of 0.113 was observed (Figure 5.27 e)). With increased strain the volume of tensile twins decreased at 250 °C and the sample deformed up to 0.3 of strain shows no significant fraction of twins (Figure 5.27 f)). Fine grains formed at high angle and twin boundaries were observed. Figure 5.28 shows the area fraction for tensile twins as a function of strain for RT and 250°C.

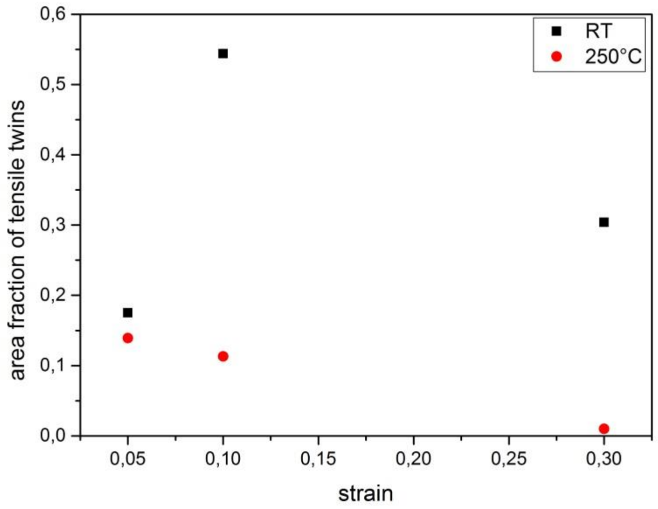

Figure 5.28: Area fraction of tensile twins as a function of strain for pure Mg at RT and 250°C

5.5.2 Recrystallization of pure Mg at 250°C

Figure 5.29 shows the GROD maps of samples deformed at 250°C up to 0.05 and 0.1 of strain.

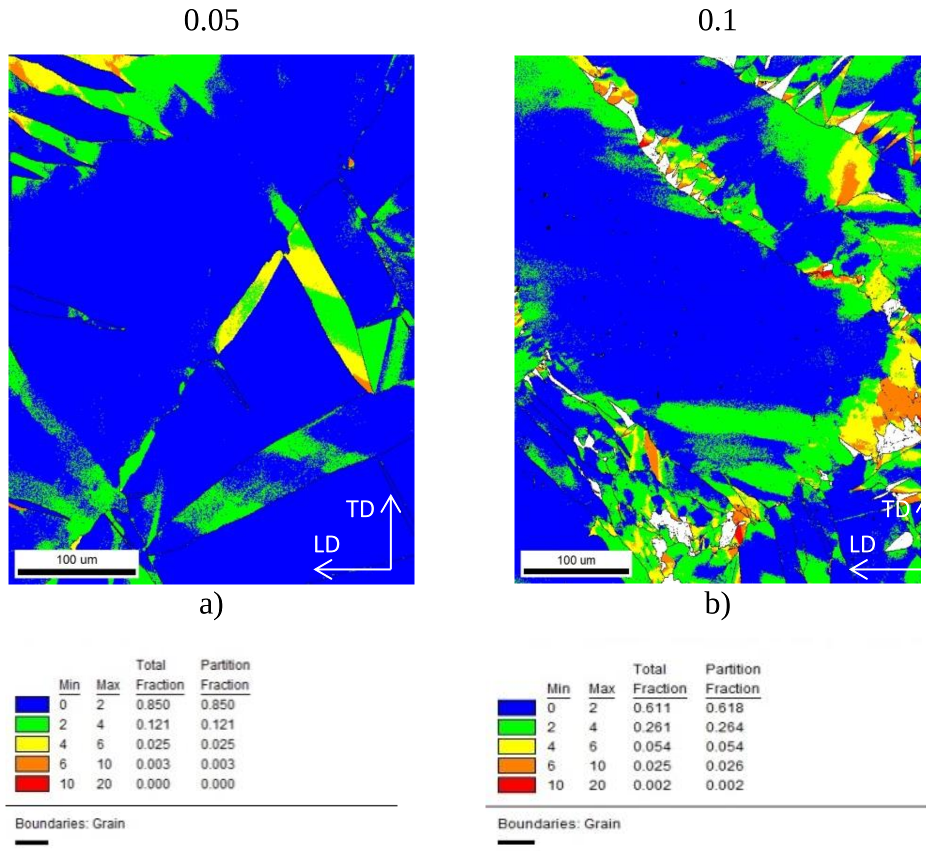

0.05 0.1

a) b)

Figure 5.29: GROD maps for pure Mg deformed up to a) 0.05 and b) 0.1 of strain at 250°C

Figure 5.29 a) shows twins with a high misorientation inside, whereas the initial matrix shows a misorientation between 0 and 2°. With continued deformation up to 0.1 of strain, the misorientation becomes higher and small grains inside formed twins were observed. Also the initial grains show indices for a continuous deformation process, marked by a transition from sub-grain formation (2-4°) to high angle boundaries (HAGBs) (10-15°°), shown in Figure 5.29 b).

Figure 5.30 a) shows that with continued compression up to 0.3 of strain a large number of fine grains are arranged at grain boundaries. The Detail in Figure 5.30 (highlighted by a star) shows a big initial grain with an increasing misorientation at a grain boundary. It was observed that this misorientation increases continuously up to a misorientation of (10-20°) or even higher marked by the white spot. The Detail in Figure 5.30 (highlighted by a triangle) shows regions of small grains arranged in a narrow line between bigger grains. The angle between initial grains around this formation was below 7°. At regions of fine grains the misorientation angles are in general low and only a few isolated grains show a very high distortion.

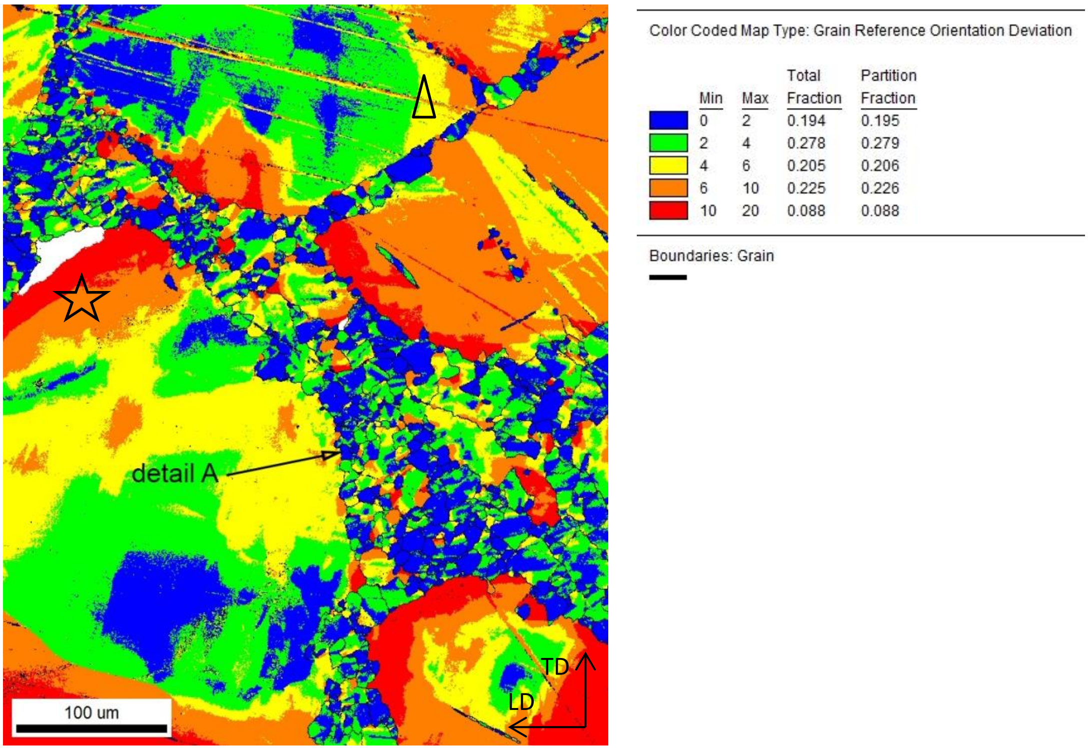

a) GROD analysis

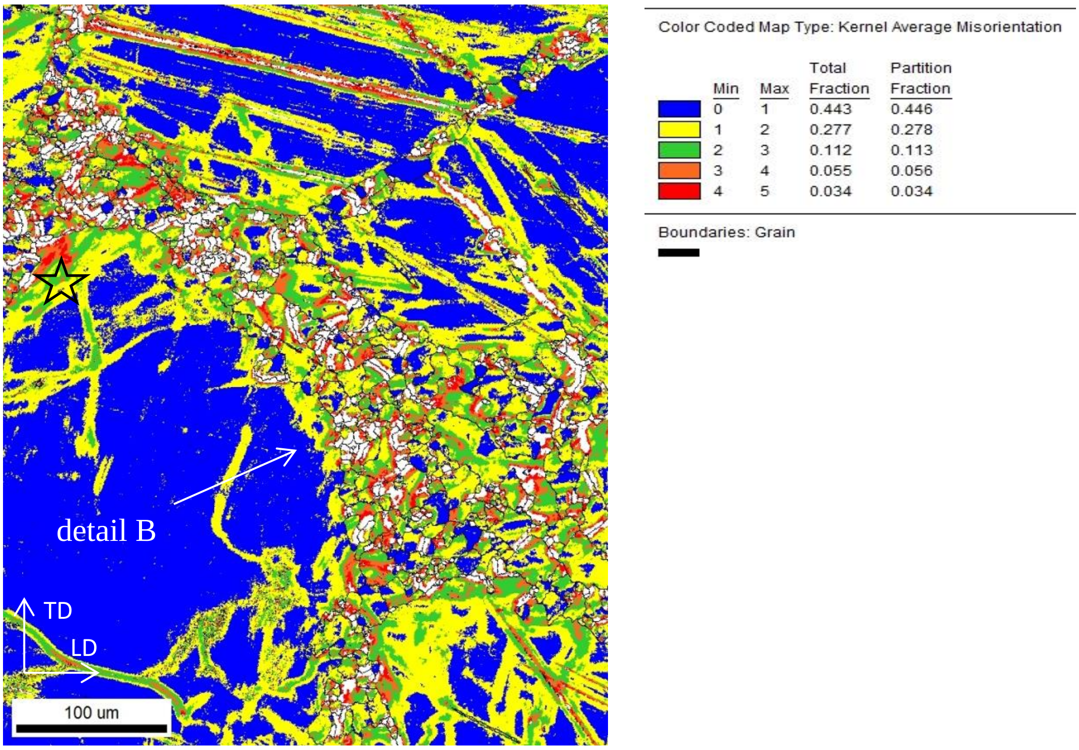

b) KAM analysis

Figure 5.30: Results of the a) GROD and b) KAM analysis for pure Mg deformed up to 0.3 of strain at 250°C

In Figure 5.30 b) the KAM analysis shows a similar morphology than the GROD analysis. In this work the 5 nearest neighbours with a maximum misorientation of 5° have been taken in consideration. It shows that the area already investigated (highlighted by a star) experiences an abrupt rise of the orientation at the grain boundary.

Detail A in Figure 5.30 a), shown in Figure 5.31, shows an area of small grains. It is noted that most of the grains reveal no significant misorientation (0-4°) and only a few a high (10-20°) misorientation.

In Detail B in Figure 5.30 b), shown in Figure 5.31, indicates that the small grains show similar characteristics than as already observed in Detail A using GROD analysis.

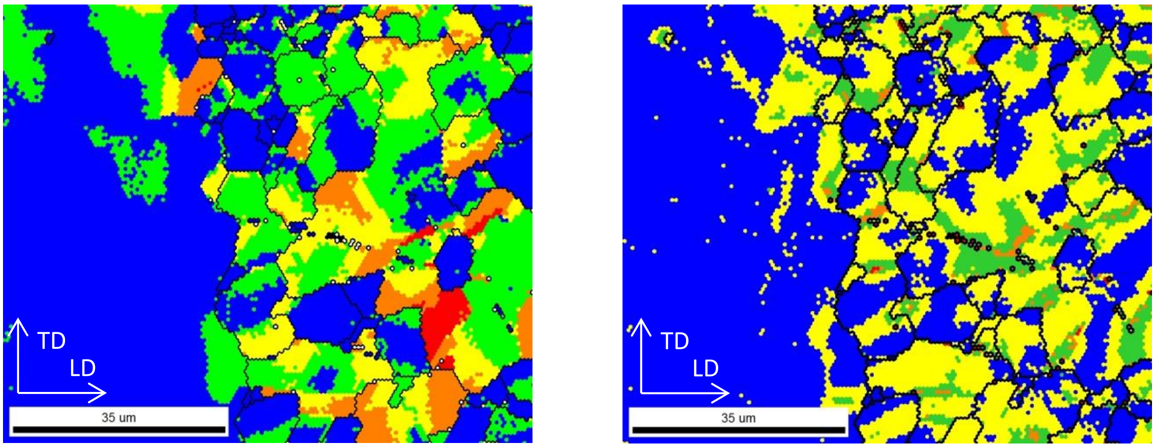

Detail A **Detail B**

Figure 5.31: Detail A using GROD a) and Detail B using KAM analysis b) for pure Mg deformed up to 0.3 of strain at 250°C

5.5.3 Deformation of ZKQX6000 alloy

Figure 5.33 shows the IPF maps of ZKQX6000 alloy after deformation at RT and 250°C. Additionally, gray scale maps are shown in Figure 5.34 to highlight twin formations.

At RT after 0.05 of strain an area fraction of 0.107 of tensile twins was measured, shown in Figure 5.34 a). Area fraction of twins at 0.1 of strain was 0.055 and decreased to 0.011 after 0.2 of strain, shown in Figure 5.34 b) and c). The samples compressed at RT showed exclusively tensile twins.

At 250°C, after 0.05 of strain an average grain size of 6.83±0.5 µm was measured, shown in Figure 5.33 d). With increased compression strain the grain size decreased, 5.12±0.6 µm for 0.1 of strain and 2.73±0.5 µm for 0.3 of strain, shown in Figure 5.33e) and f). No twinning was observed at 250 °C (Figure 5.34 d), e) and f)). An overview of the area fraction of tensile twins as a function of strain is illustrated in Figure 5.32.

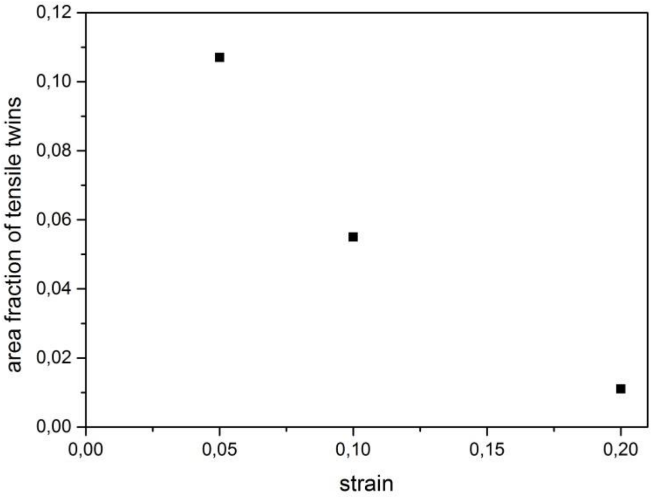

Figure 5.32: Area fraction of tensile twins as a function of strain for ZKQX6000 alloy at RT

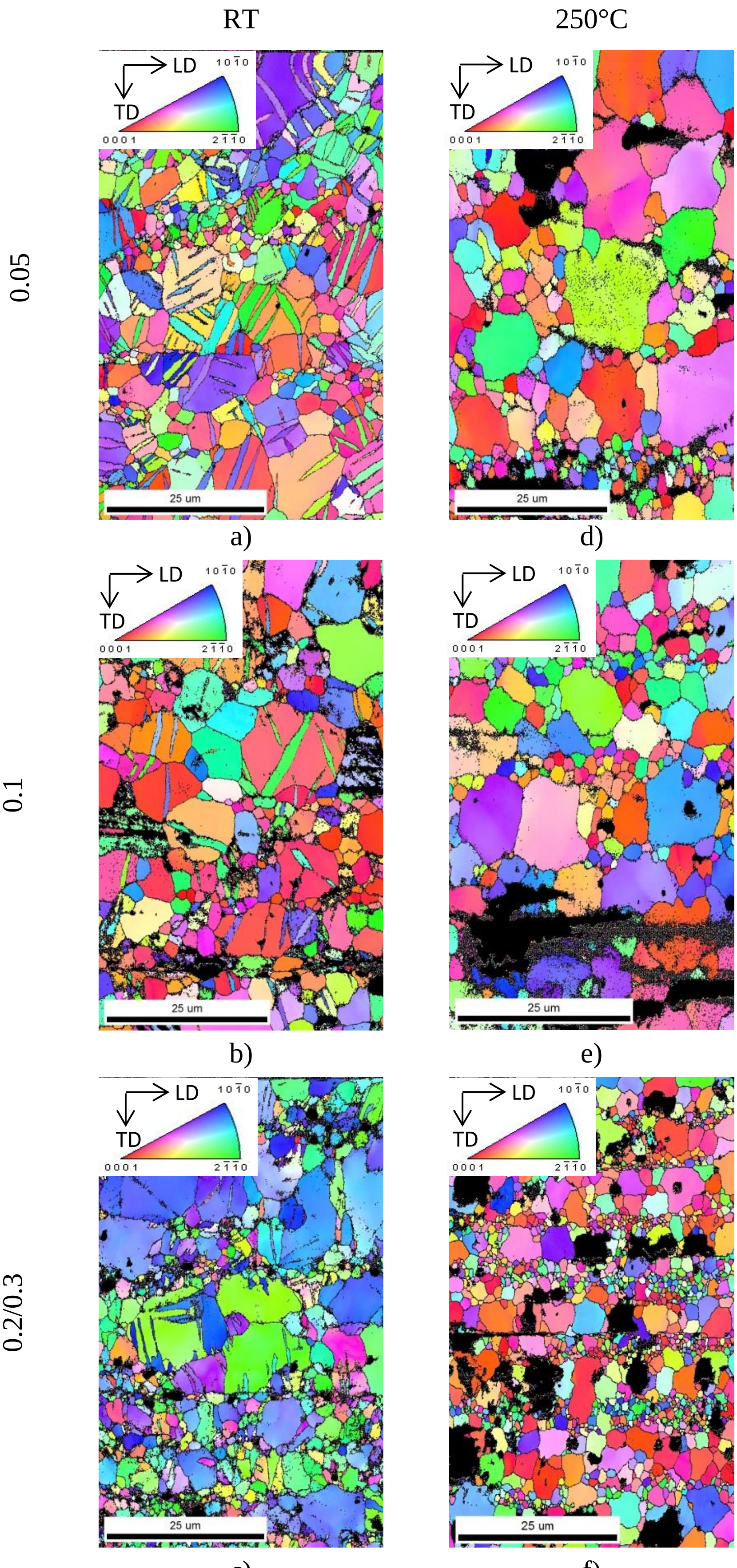

a) b) c) d) e) f)

Figure 5.33: IPF maps of ZKQX6000 alloy showing grain boundaries and twins up to a) 0.5 b) 0.1 c) 0.3 of strain at RT and d) 0.5 e) 0.1 f) 0.3 of strain at 250°C

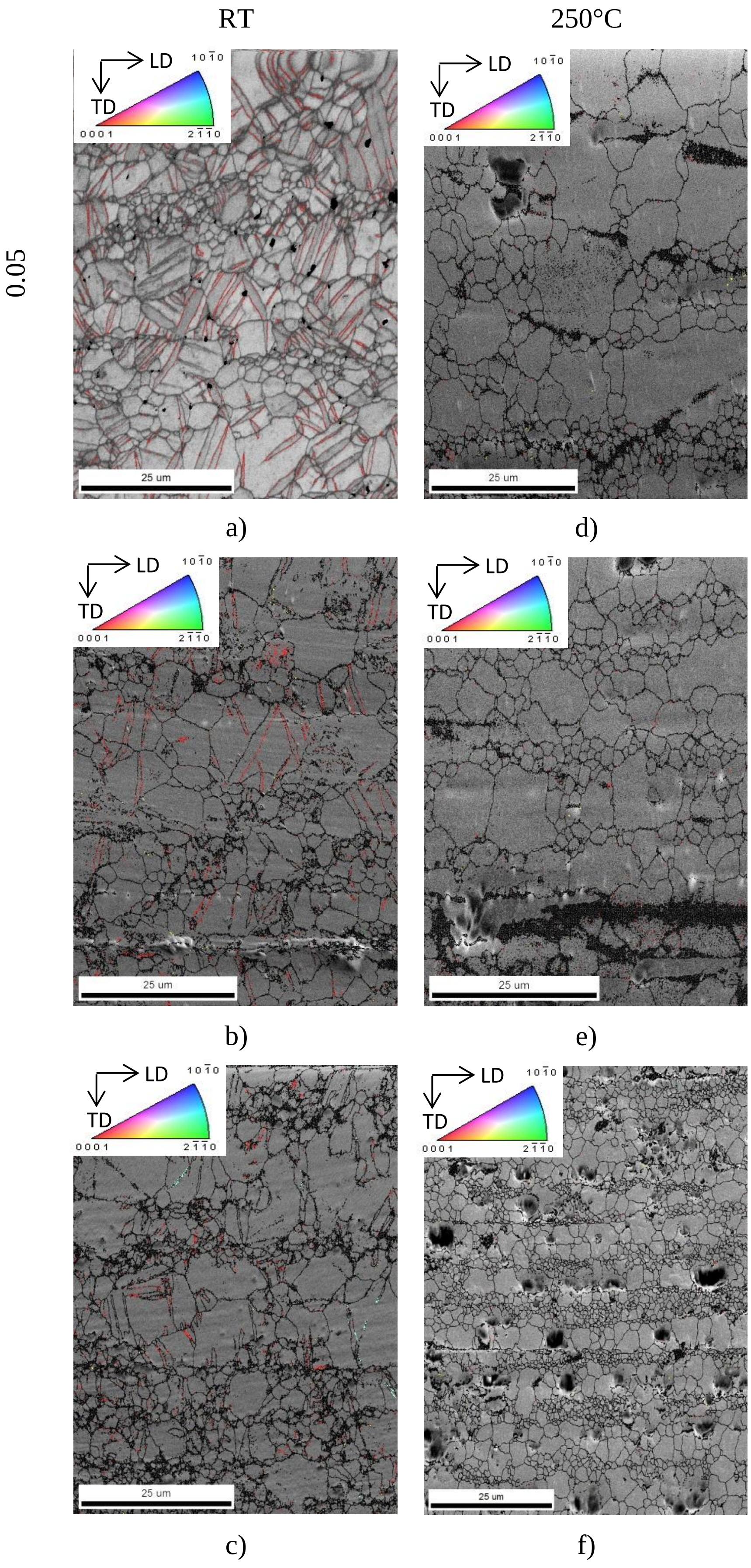

Figure 5.34: Gray scale maps of ZKQX6000 alloy showing grain boundaries and twins up to a) 0.5 b) 0.1 c) 0.3 of strain at RT and d) 0.5 e) 0.1 f) 0.3 of strain at 250°C

5.5.4 Recrystallization of ZKQX6000 alloy

At a temperature of deformation of 250°C the grain size decreases with increased strain. Figure 5.35 illustrates the GROD analysis for the samples compressed at 250°C up to different strains. In the sample deformed up to 0.05 of strain the misorientation inside the grains is high and the area fraction region with a misorientation between 2 to 10° is 0.272, shown in Figure 5.35 a).With increased strain the misorientation within the grains decreases rapidly and the area fraction is 0.064 after a strain up to 0.3, shown in Figure 5.35 c). In general, it can be seen that with increasing the deformation the number of small grains increases. To identify recrystallized grains a GROD and a KAM analysis were performed at a higher magnification from regions selected in Figure 5.35 and are shown in Figure 5.36.

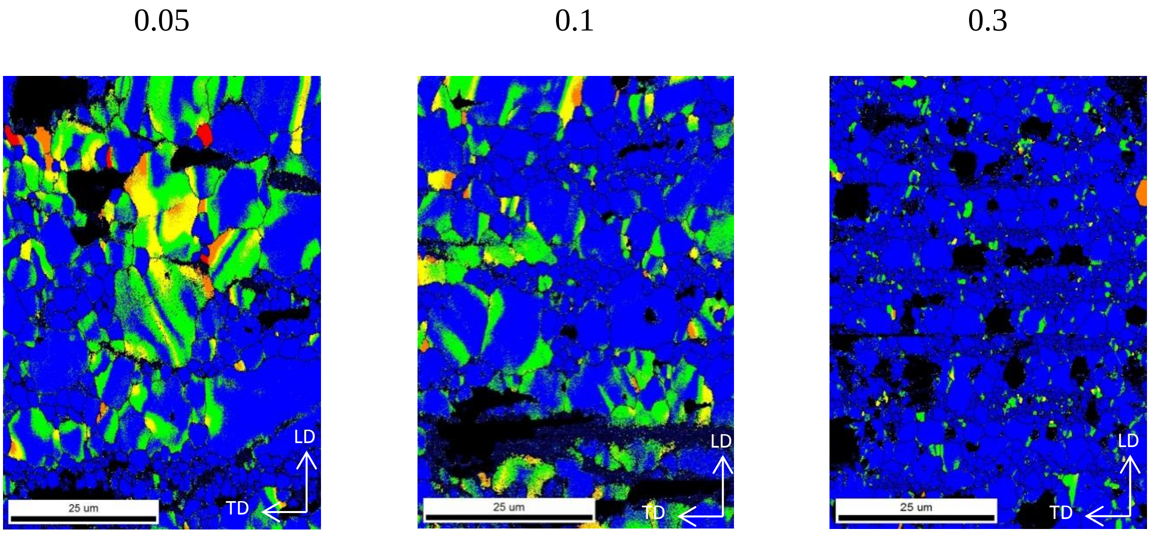

a) b) c)

Color Coded Map Type: Grain Reference Orientation Deviation

	Min	Max	Total Fraction	Partition Fraction
🟦	0	2	0.638	0.638
🟩	2	4	0.195	0.195
🟨	4	6	0.061	0.061
🟧	6	10	0.016	0.016
🟥	10	20	0.003	0.003

Boundaries: Grain

Color Coded Map Type: Grain Reference Orientation Deviation

	Min	Max	Total Fraction	Partition Fraction
🟦	0	2	0.660	0.660
🟩	2	4	0.196	0.196
🟨	4	6	0.046	0.046
🟧	6	10	0.014	0.014
🟥	10	20	0.001	0.001

Boundaries: Grain

Color Coded Map Type: Grain Reference Orientation Deviation

	Min	Max	Total Fraction	Partition Fraction
🟦	0	2	0.795	0.795
🟩	2	4	0.051	0.051
🟨	4	6	0.009	0.009
🟧	6	10	0.004	0.004
🟥	10	20	0.000	0.000

Boundaries: Grain

Figure 5.35: GROD analysis for the ZKQX6000 alloy deformed up to a) 0.05 b) 0.1 and c) 0.2 of strain at 250°C

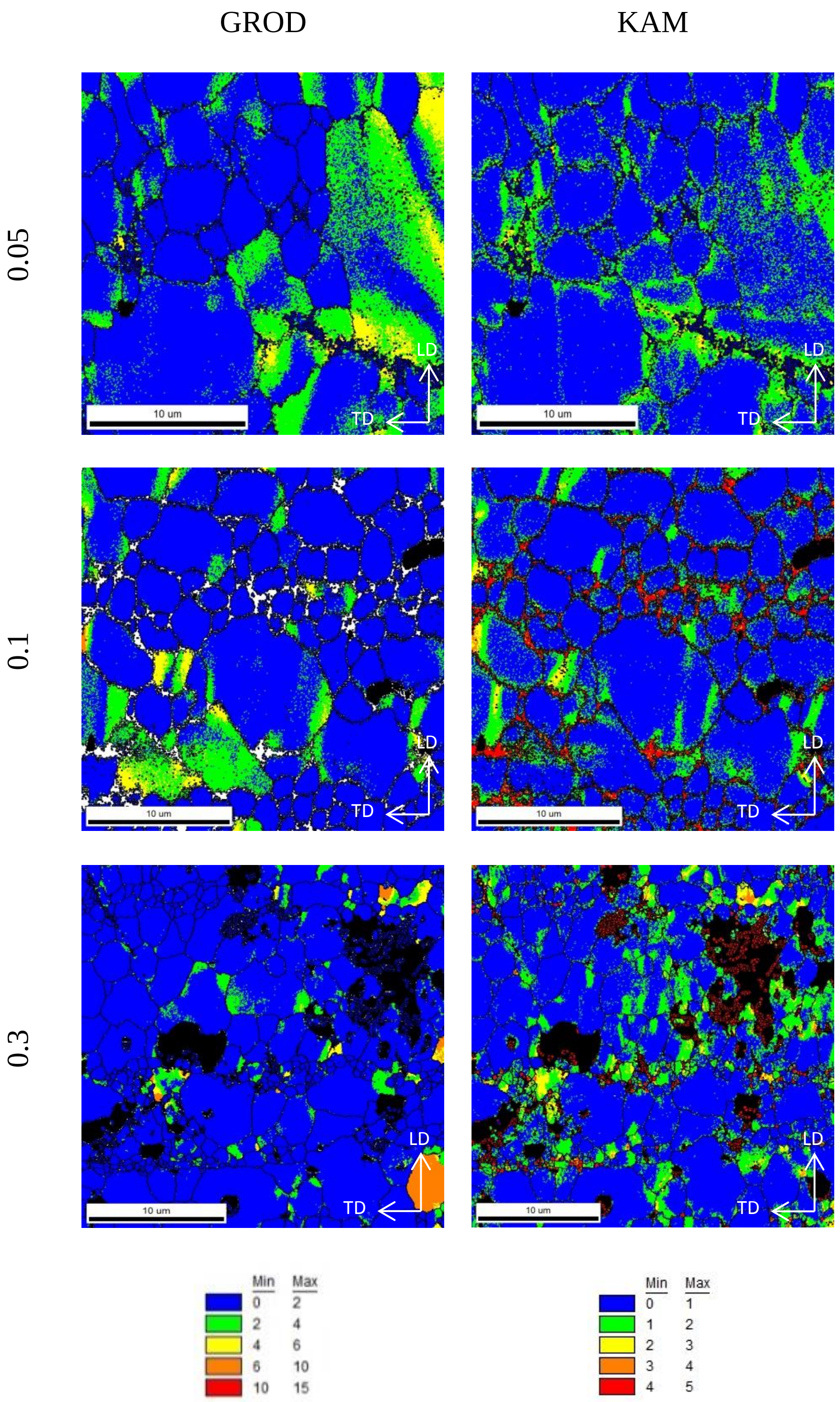

Figure 5.36: GROD and KAM analysis after different strains at 250°C selected in Figure 5.35

Regarding the GROD analysis in Figure 5.36 the sequence reveals a decrease of a misorientation inside the grains with increased strain. The KAM analysis shows the misorientation deviation for low angles. At 0.05 of strain misorientation preferably at grain boundaries was observed. With continued strain a fragmented deviation of distorted grains was detected.

6 Discussion and conclusions

6.1 Cold deformation and twin formation

During cold deformation of Mg and Mg alloys at RT the CRSS to activate prismatic and pyramidal slip is high (Figure 3.11 and Figure 3.14). In order to reduce the strain in the matrix, twinning occurs.

The flow curve of pure Mg sample (grain size 1193±25 µm) at RT shows in Figure 5.5 a yield strength of 15 MPa and a maximum stress of 130 MPa at a deformation up to 0.3 of strain. After yielding at a deformation of 0.02 of strain, a change in the slope in the stress was observed due to twinning. Sigmoidal twinning-dominated flow is correlated to a significant change in concavity and followed by a rapid hardening. In the strain hardening region a high strengthening effect is noticed caused by progressive twinning (Molodov et al. 2014). This was also observed by investigating the intensity changes of the synchrotron diffraction. A significant change in the (0002)-basal-$\{10\bar{1}0\}$-prismatic planes was noted, in the moment when deformation started (

Figure 5.7). It is noteworthy to mention that the results for pure Mg are not comprehensible and this can be explained by the coarseness of Mg. High intensity bounds may be a result of the reflection of new grains, which extend into the beamline during deformation or can be charged to the influence of the absorber. But nevertheless, the line profiles provide useful information about twinning mechanisms by showing a general trend of intensity changes.

The microstructures investigated by using LOM show that with increased strain, the area fraction of twins increases (Figure 5.13, Figure 5.14 and Figure 5.15). In Figure 5.27, showing the gray scale maps including the area fraction of twins, a similar observation has been made. Exclusively tensile twins were observed and an increased area fraction of twins with continued strain.

A DRX mechanism was not observed for the pure Mg at RT, but the A-T plots show evidences for an *in situ* grain rotation and misorientation within the grains, followed by a final texture. The A-T plots for pure Mg shows diffraction lines which are bending when compression starts (Figure 5.8). This bending is related to a grain rotation, followed by a broadening or blur for continued compression. The broadening and blur of the diffraction lines show that accumulated strain inside the grains increases and involves an increment of misorientation within the grains. The yellow arrows in Figure 5.8 are showing representative examples for a grain misorientation. It can be seen, that parts of the grain experience a high misorientation, marked by a splitting of the diffraction lines.

The ZKQX6000 alloy has a mean grain size of 6.9±1 µm when measuring with LOM and 7.1±1 µm if EBSD analysis is done. The alloy shows indices for twinning while deforming. A yield strength of 190 MPa and an maximum stress of 410 MPa at a deformation up to 0.3 of strain was measured. After yielding at a true strain of 0.025, as already observed for the pure Mg, a change of the slope in the flow curve is observed, related to twinning. This confirmed by the investigations of the intensity changes (Figure 5.10), where a continuous change up to 0.3 of strain between the (0002)-basal-$\{10\bar{1}0\}$-prismatic planes was observed. Contrary to the pure Mg, the ZKQX6000 alloy shows a decreasing area fraction of twins by increasing the deformation at RT. Both the EBSD analysis (Figure 5.34) and the LOM analysis (Figure 5.20 to Figure 5.22) reveal this characteristic.

At RT, up to 0.3 of strain the ZKQX6000 alloy does not show evidences of DRX. The grain size stayed constant with increasing deformation and no mosaic spread of the diffracted lines was observed (Figure 5.11) in the A-T plots. In general, a deformation mechanism, in terms of grain rotation or misorientations inside the grains, was hard to detect due to small grain size which produces continuous Debye-Scherrer lines.

6.2 Deformation at 250°C and recrystallization

In pure Mg at 250°C, twinning was detected after yielding, leading to not distinctive strengthening effect in the strain hardening region. A yield stress of 8 MPa and a maximum stress of 50 MPa deformed up to 0.3 of strain was measured. Investigating the intensity changes of the *in situ* measurements (Figure 5.7 e)) confirm the results of the flow curves. For deformation up to 0.5 of strain a change in intensity between the (0002)-basal-$\{10\bar{1}0\}$-prismatic planes was noted, followed by absence of twinning after a deformation higher than 0.1 of strain. The microstructures confirm this behaviour. After deformation to 0.05 of strain the volume fraction of twins is low, but it can be observed that these twins show a wide base. Additionally it was observed, that twins are preferentially formed at some specific crystallographic orientations (Figure 5.16). At deformation up to 0.3 of strain no twins were observed in the microstructure. Also the EBSD analysis shows a decreasing area fraction of tensile twins as a function of strain (Figure 5.28). The decrease of twinning can be explained by the ease of activation of prismatic and pyramidal planes at elevated temperatures, with reference to Figure 3.11.

Furthermore, it was observed that DRX, characterized by a peak stress of the flow curve (Figure 5.5 e)), occurs after twinning at a strain of approximately 0.1. This can also be revealed exclusively in the microstructures deformed up to 0.3 of strain (Figure 5.18), where an accumulation of small grains was observed. By using EBSD analysis it was possible to investigate the process of DRX in detail. It is noted that at 0.1 of strain DRX occurs preferably inside previous formed twins (Figure 5.29 b)). At a deformation up to 0.3 of strain (Figure 5.30), evidences for CDRX, DDRX and TDRX were found. A representative area (highlighted by a star) shows a possible CDRX with an increasing misorientation at the grain boundaries. In regions of fine grains, grains with no misorientation inside were observed, related to a DDRX. In the area (highlighted by a triangle) the angle between initial bordering grains around the new formation was below 7°, which can be a sign for a primary twin. This may also be the reason for a lower area fraction of twins with increasing strain. By noting the A-T plots, it was possible to proof the deformation sequence *in situ*. It was found that in the beginning of deformation, the diffraction lines start to bend (grain rotation) and blur (high misorientation within the grain), followed by a mosaic spread (DRX).

The flow curve of the ZKQX6000 alloy deformed up to 0.3 of strain does not show any change in slope of the flow curve, meaning that twins are not activated at this temperature. The peak stress was spotted at 48 MPa followed by a softening effect. In both the LOM analysis (Figure 5.25) and the EBSD analysis (Figure 5.34) no evidences for twinning were found. On the other hand a change in intensities between the (0002)-basal-$\{10\bar{1}0\}$-prismatic and the $\{11\bar{2}0\}$-prismatic–$\{10\bar{1}3\}$-pyramidal 3rd order was observed (Figure 5.10 e)). This insignificant intensity change should play a minor role in the activation of twinning. With reference to Figure 3.14 it can be seen that the CRSS for activating twins increases for Zn containing alloys at elevated temperatures.

Figure 6.1 shows the grain size as a function of strain for the ZKQX6000 alloy. The EBSD results are deviating from the LOM measurements. This can be explained by the fact that the observed area for the EBSD analysis (max. 80 x 80 µm) is not statistical reliable. Dispersion bands out of the initial structure which appear on the observed area influence the average grain size essentially. On the other hand the results of the LOM only consider a change in the shape of grains in LD under deformation (section 4.3.2).

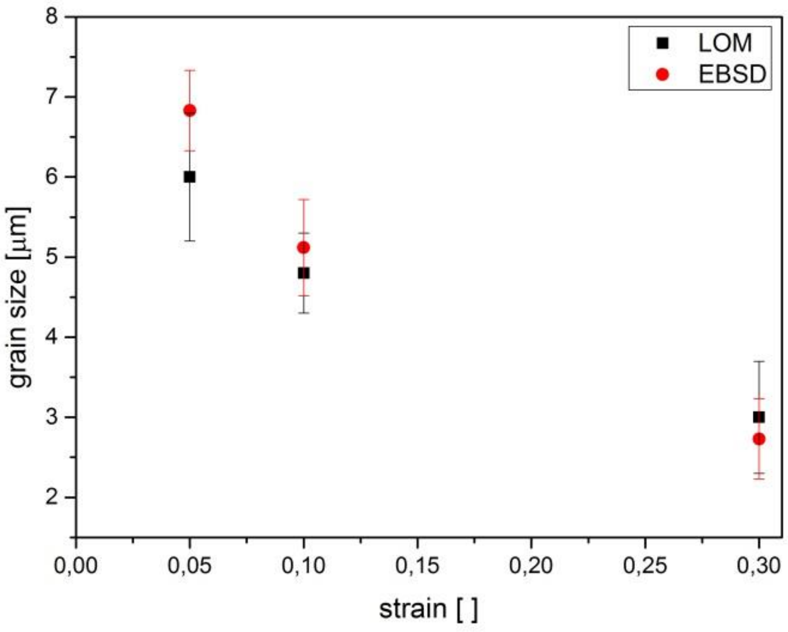

Figure 6.1: Grain size as a function of strain for the ZKQX600 alloy

The decrease of the grain size with increased strain confirms the DRX. With reference to Figure 5.35, using GROD analysis, it can be seen that the sample deformed up to 0.05 of strain reveals a high amount of misorientation. This misorientation is associated with high strain inside the grains, promoting the recrystallization processes at lager strains. By increasing the strain up to 0.1 the misorientation shows a lower density. Small grains near grain boundaries are observed, leading to the assumption that DRX occurs. Deformation up to 0.3 of strain indicates that the misorientation inside the grains become even lower combined with a high volume of recrystallized grains. The same process was observed in the A-T plots. At 0.001 of strain a high misorientation was noted, followed by DRX with appropriated spreading of the diffraction lines at 0.1 of strain.

By comparing the pure Mg and the ZKQX6000 alloy it can be concluded, that due to both the difference of the grain size and the influence of the alloying elements in CRSS, the sequence in deformation mechanisms are different. Therefore, the strain reduction of big grains as in pure Mg is difficult, thus twinning occurs first. In contrast, in the ZKQX6000 alloy an earlier strain reduction is observed, leading to DRX.

The absence of twinning, the higher CRSS to activate basal slip of the ZKQX6000 compared to pure Mg (Figure 3.12) and the lower CRSS to activate prismatic slip (Figure 3.13), may be responsible for the characteristic flow curve. Also an important role may play the activation of the DRX in the ZKQX6000 alloy. The DRX may be appropriate for the increased yield stress, through stress reduction in the crystal´s lattice, and the smooth softening process after yielding.

6.3 General remarks

In this work the predominating deformation mechanisms of the ZKQX6000 alloy compared to pure Mg could be satisfyingly clarified. The unique combination of traditional techniques such as LOM, EBSD and flow analysis with *in situ* X-Ray diffraction by means of synchrotron sources resulted in an explanation and description of deformation mechanisms in pure Mg and a Zn rich Mg alloy.

The use of synchrotron provides information about the deformation mechanisms in crystalline materials as a function of the deformation grade, not achieved by post-mortem samples. In this work, the analysis of peak intensities and A-T plots was useful to describe the activity of slip planes and microstructure evolution by increasing the strain. Although the interpretation of the diagrams is not an easy task, they have large potential for the analysis of deformation mechanisms.

7 Outlook

The experimental methods were consistently. However, some of the results could not be fully explained. Despite all expectations, the area fraction of twins of the ZKQX6000 alloy decreased with increased strain at RT. One possible explanation could be the difference of the initial textures between the investigated samples, which make it hard to identify twins. Another reason may be the fact that the growing twins consume whole grains with increased deformation.

For further research, it might be appropriate to consider a minimisation of the grain size of pure Mg by means of extrusion. This would have a positive effect on the results of the *in situ* synchrotron diffraction investigations. Furthermore, it would be of interest to investigate the deformation behaviour between RT and 250°C to understand the mechanism of deformation better.

8 Bibliography

Agnew, S.R., Yoo, M.H. & Tome, C.N., 2001. Application of texture simulation to understand mechanical behavior of Mg and solid solution alloys containing Li or Yi. *Acta Materialia*, 49, pp.4277–4289.

Akhtar, T. & Teghtsoonian, E., 1969a. Solid solution strengthening of magnesium single crystals-I Alloying behaviour in basal slip. *Acta. Metall.*, 17, p.1339.

Akhtar, T. & Teghtsoonian, E., 1969b. Solid solution strengthening of magnesium single crystals-II Alloying behaviour in prismatic slip. *Acta Metall.*, 17(11), pp.151–1356.

Al-Samman, T., 2008. *Magnesium - The Role of Crystallographic Texture*. TH Aachen.

Als-Nielsen, J., 2010. *Elements of Modern X-ray Physics* 2nd ed., Wiley.

Barnes, P., 2006. How does synchrotrons work? *Birkbeck College, London*. Available at: http://pd.chem.ucl.ac.uk/pdnn/inst2/work.htm [Accessed May 7, 2014].

Barnett, M., 2004. Influence of grain size on the compression deformation of wrought Mg-3Al-1Zn. *Acta Materialia*, 52, pp.5093–5103.

Barnett, M., 2007. No Title. *Materials Science & Engineering A 464*, pp.1–16.

BMU, 2010. Eu Verordnung Co2 PKW. , p.1. Available at: http://www.bmu.de/fileadmin/bmu-import/files/pdfs/allgemein/application/pdf/eu_verordnung_co2_emissionen_pkw.pdf [Accessed November 25, 2013].

Brünglinghaus, C., 2012. Magnesium - Konkurrenz für Polymerwerkstoffe und Aluminium. *www.springerprofessional.de*, p.1. Available at: http://www.springerprofessional.de/magnesium-konkurrenz-fuer-polymerwerkstoffe-und-aluminium/3156328.html [Accessed November 25, 2013].

Doherty, R.D. et al., 1997. Current issues in recrystallization: a review. *Materials Science and Engineering: A*, 238(2), pp.219–274. Available at: http://linkinghub.elsevier.com/retrieve/pii/S0921509397004243.

Galiyev, A., Kaibyshev, R. & Gottstein, G., 2001. Correlation of plastic deformation and dynamic recrystallization in magnesium alloy ZK60. *Acta Materialia*, 49(7), pp.1199–1207.

Gottstein, G., 2007. Der automistische Aufbau der Festkörper. In *Materialkunde, Physikalische Grundlagen der Materialkunde*. Aachen: Springer, pp. 11–55,197–288,303–355.

Homayonifar, M., 2011. Modeling of deformation-induced twinning and dislocation slip in Magnesium using a variationally consistent approach.

Ion, S.E., 1982. Dynamic recrystallisation and the development of microstructure during the high temperature deformation of magnesium. *Acta Metallurgica*, 30(10), pp.1909–1919. Available at: http://linkinghub.elsevier.com/retrieve/pii/0001616082900311.

Jain, A. & Agnew, S.R., 2007. Modeling the temperature dependent effect of twinning on the behavior of magnesium alloy AZ31B sheet. *Materials Science and Engineering: A*, 462(1-2), pp.29–36. Available at: http://linkinghub.elsevier.com/retrieve/pii/S0921509306018739 [Accessed March 19, 2014].

Jinxiang, X., 2014. Proceedings of the IMA 2014 World Conference. In pp. 4–9.

Koike, J., 2003. The activity on non-basal slip systems and dynamic recovery at room temperature in fine-grained AZ31B magnesium alloys. , 51(7), pp.2055–2065.

Liss, K., Li, H., et al., 2009. No Title. *Adv. Eng. Mater*, 11:637340.

Liss, K., Yan, K., et al., 2009. No Title. *Appl. Phys.*, 106:11e526.

Liss, K. & Yan, K., 2010. No Title. *Mater Sci. Eng. A*, 528:11e27.

Lou, X. et al., 2007. Hardening evolution of AZ31B Mg sheet. *International Journal of Plasticity*, 23(1), pp.44–86. Available at: http://linkinghub.elsevier.com/retrieve/pii/S0749641906000398 [Accessed December 19, 2013].

Mendis, C.L. et al., 2009. Precipitation-hardanable Mg-2.4Zn-0.1Ag-0.1Ca-0.16Zr (at/%) wrought magnesium alloy. *Acta Materialia*, 57(3), pp.749–760. Available at: http://dx.doi.org/10.1016/j.actamat.2008.10.033.

Mendis, C.L. & Hono, K., 2007. Enhanced age hardening in a Mg – 2 . 4 at .% Zn alloy by trace additions of Ag and Ca. , 57, pp.485–488.

Von Mises, R., 1928. Mechanik der plastischen Formänderung von Kristallen. *Zeitschrift für angewandte Mathematik und Mechanik*, 6, pp.161–183.

Miura, S., 2004. *unpublished research*, Japan: Hokkaido University.

Moffatt, W., 1964. *The structure and properties of materials* 1st ed., New York: John Wiley & Sons.

Molodov, K.D. et al., 2014. On the Ductility of Magnesium Single Crystals at Ambient Temperature. *Metallurgical and Materials Transactions A*. Available at: http://link.springer.com/10.1007/s11661-013-2152-6.

Müller, S., 2007. *Weiterentwicklung des Strangpressens von AZ Magnesiumlegierungen im Hinblick auf eine Optimierung der Mikrostruktur , des Gefüges und der mechanischen Eigenschaften*. Technische Universität Berlin.

Obara, T., 1973. {1122}{1123} slip system in magnesium. *Acta Metall.*, 21.

Oh-ishi, K. et al., 2009. Bimodally grained microstructure development during hot extrusion. *Acta Materialia*, 57(18), pp.5593–5604. Available at: http://dx.doi.org/10.1016/j.actamat.2009.07.057.

Oxford Instruments, 2013. Principal System Components. *Basic of EBSD*. Available at: www.ebsd.com [Accessed February 24, 2014].

Polmear, I., 2006. *Light Alloys* 4th ed., Oxford: Elsevier.

Raynor, G. V., 1959. *The Physical Metallurgy of Magnesium and its alloys*, Oxford: Pergamon Press.

Roberts, C.S., 1964. *The deformation of magnesium. Magnesium and its Alloys*, New York: Wily.

Schmid, E., 1968. *Plasticity of Crystals* W. Boas, ed., London: Chapman & Hall Ltd.

Schmoelzer, T., Liss, K. & Staron, P., 2011. No Title. *Adv. Eng. Mater*, 685e99.

Sitdikov, O., 2001. Dynamic Recrystallization in pure magnesium. *Materials Transactions*, 42(9), pp.1928–1937.

Struers, 2008. Sicherheitsdatenblatt. Available at: www.struers.de/resources.

Taylor, G.I., 1938. *Plastic strain in metals*, Journal Institute of Metals 62.

Wonsiewicz, B.. & Backofen, W.A., 1967. No Title. *Transactions of the Metallurgical Society of AIME*, 239.

Yin, D.L. et al., 2005. Warm deformation behavior of hot-rolled AZ31 Mg alloy. , 392(September 2004), pp.320–325.

Yoo, M.H., 2002. Nonbasal deformation Modes of hcp metals and alloys. In *Role of dislocation source and mobility*. Metallurgical and materials transactions A, pp. 813–822.

Yoo, M.H., 1981. Slip, Twinning, and Fracture in Hexagonal Close-Packed Metals. *Metallurgical Transactions A*, 12(3), pp.409–418.

9 List of figures

10 List of tables

11 Appendices

11.1 Appendix I

Initial and final lengths of undeformed samples

	initial length [mm]						
	RT				250 °C		
Strain	**5%**	**10%**	**20%**	**30%**	**5%**	**10%**	**30%**
Pure Magnesium							
Sample 1	9,97	9,835		9,99	10,1	10,15	10,08
Sample 2	9,97	9,9694		9,81	9,99	10,08	10,01
Sample 3				9,99			10,05
ZKQX6000							
Sample 1	10,15	11,41	10,63		10,21	9,8	9,45
Sample 2	9,66	10,55	10,9		11,24	10,1	10,6
Sample 3			10,81				9,66

	final length [mm]						
	RT				250 °C		
Strain	**5%**	**10%**	**20%**	**30%**	**5%**	**10%**	**30%**
Pure Magnesium							
Sample 1	9,55	9,10		**	9,60	9,10	7,2
Sample 2	9,60	9,10		**	9,50	9,10	7,05
Sample 3				**			7,1
ZKQX6000							
Sample 1	9,80	9,80	**		9,70	8,90	6,70
Sample 2	9,30	9,70	**		9,80	10,10	7,50
Sample 3			**				6,85
	final central diameter [mm]						
	RT				250 °C		
Strain	**5%**	**10%**	**20%**	**30%**	**5%**	**10%**	**30%**
Pure Magnesium							
Sample 1	5,15	5,20		**	5,35	5,30	5,7*
Sample 2	5,00	5,10		**	5,25	5,30	6,45*
Sample 3				**			6,7*
ZKQX6000							
Sample 1	5,00	5,00	**		5,05	5,25	6,05
Sample 2	5,10	5,20	**		5,00	5,05	6,1
Sample 3			**				6,1

*high deformation (imprecise values)

**broken

11.2 Appendix II

2θ-intensity curves

Pure Mg:

RT 250°C

0.05

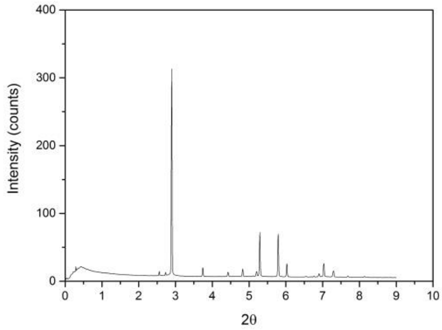

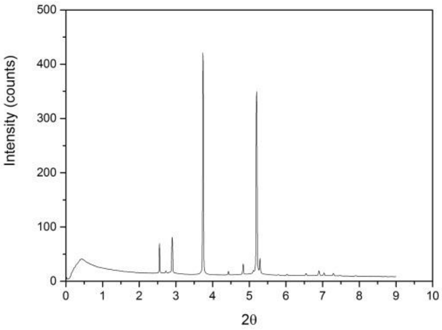

0.1

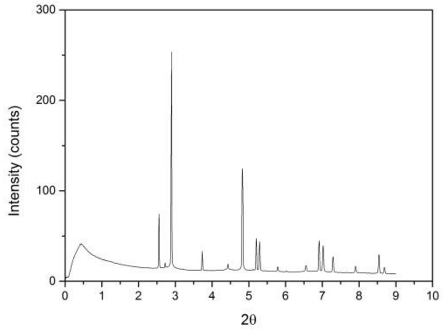

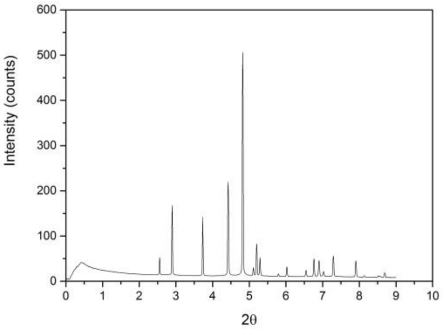

0.3

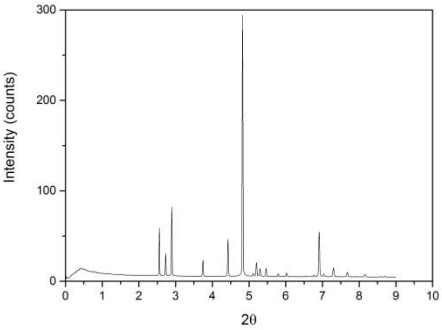

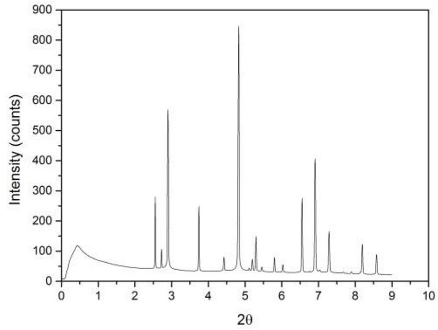

ZKQX6000 alloy:

RT

250°C

0.05

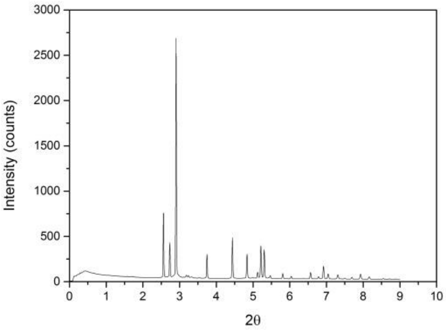

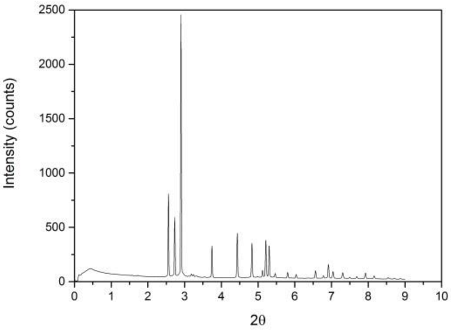

0.1

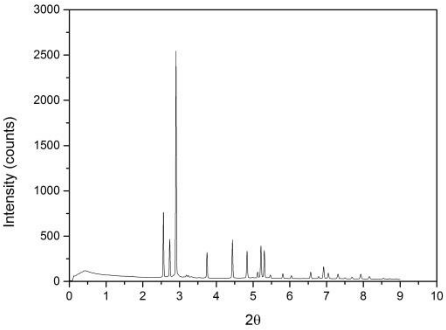

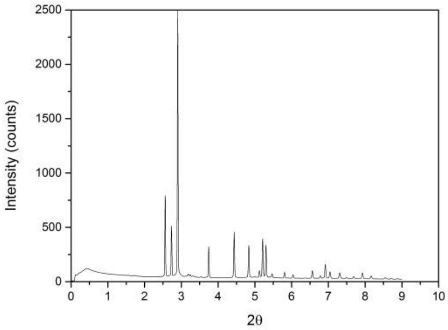

0.2/0.3